11PFL-0091
SAND2010-7861C

Relationship between diesel fuel spray vapor penetration/dispersion and local fuel mixture fraction

Author, co-author (Do NOT enter this information. It will be pulled from participant tab in MyTechZone)
Affiliation (Do NOT enter this information. It will be pulled from participant tab in MyTechZone)

ABSTRACT

The fuel-ambient mixture produced by sprays is fundamental to the performance and operation of engines. Unfortunately, experimental difficulties limit the direct measurement of local fuel-ambient mixture, inhibiting quantitative assessment of mixing. On the other hand, measurement of global quantities, such as the spray penetration rate, is relatively straightforward. Simplified models to predict local fuel-ambient mixture have also been developed, based on these global parameters. However, experimental data to validate these models over a range of conditions is needed. In the current work, we perform measurements of spray global quantities such as vapor-phase penetration, liquid-phase penetration, spreading angle, and nozzle flow coefficients over a range of conditions in a high-temperature, high-pressure vessel. Using this data, we exercise the Musculus and Kattke model for prediction of fuel mixture fraction and compare to quantitative mixing measurements performed by Rayleigh scattering in the vaporized portion of the spray. Results show that spreading angles based on measurement of the most sensitive outer boundary of the spray, by schlieren or Rayleigh-scatter imaging, are needed as inputs to the model to obtain a match between modeled and measured fuel spray penetration rates. Using this same spreading angle, the model predictions also produce local mixture fractions that are within the Rayleigh scattering experimental uncertainty. Accurate model predictions of mixture fraction are achieved for a range of ambient densities, fuel injector nozzle shapes, injection pressures, and types of fuels. Extrapolation of the mixing measurements suggests that a fuel spray has a smaller spreading angle in the near-field and transitions to a larger angle in the far-field.

INTRODUCTION

Controlled fuel-air mixing from sprays is key to combustion optimization in engines. However, currently there are many shortcomings in our understanding of sprays and the type of fuel-ambient mixtures produced in engines. For diesel or low-temperature combustion engines, some of the most basic aspects of sprays, including the spray penetration rate and spreading angle, are not fully repeatable from injector-to-injector, or even from hole-to-hole of an individual injector. Causes for these variations likely originate from internal injector and nozzle flows, but these processes are not well understood. As such, CFD models for spray breakup and dispersion are not completely predictive. Indeed, a review of CFD engine simulation capability calls spray modeling the major uncertainty [1].

Because of current limitations in our understanding of sprays, experimentation is required to better characterize sprays for model validation. Often, measurements of spray penetration and spreading angle are used to calibrate the CFD sub-models for the spray. Probably the most common experimental setup for these types of measurements is a pressurized spray chamber operating at room temperature. While many aspects of fuel injection in an operating engine are likely represented, there are several problems with interpretation of data from this type of experiment. First, since a room-temperature spray is essentially non-evaporating, difficulties arise when attempting to derive fuel mass concentration from droplets of different diameter and number density. The relationship of scattered or extinguished light from droplets to fuel concentration is difficult to quantify, particularly in the dense region near the nozzle. Without quantification, the "boundary" of the spray can be difficult to define as it relates to spreading angle or penetration. Second, the mixing processes in this room temperature experiment may be different than those in the high-temperature, high-pressure in-cylinder engine environment. Droplets in diesel fuel sprays injected into gases at high temperature and pressure will vaporize and create a different physical environment in which mixing occurs. For these reasons, spray chambers have been developed that operate at elevated pressures and temperatures typical of an engine. A recent review of these facilities is found in [2].

Even for chambers that operate at high pressure and temperature, measurements of the spray penetration and spreading angle are ubiquitous in the literature. Simplified spray models derived from these data are also fairly common. As such, we will review several experimental observations and spray modeling approaches from our own group for which we have the most experience. The general experimental observations and spray modeling experience are shared, at least in part, by a number of other investigators.

Using high-speed schlieren imaging, Naber and Siebers [3] compared the penetration and spreading angle of evaporating (high-temperature) and non-evaporating (low-temperature) sprays over an extensive range of gas densities, even surpassing that typically experienced in an engine (3-60 kg/m^3). The dataset also included data for a range of injection pressures (76-160 MPa), injector nozzle orifice diameters (0.198-0.340 mm), and elevated ambient temperatures (600-1400 K). They showed that the spray penetration slows, as expected, with increasing ambient gas density, and that the density effect on penetration partly occurs as a result of the effect of ambient density on the spray spreading angle (*i.e.*, spray air entrainment and mixing). They also found that the penetration rate and spreading angle of an evaporating spray were both lower than that of a non-evaporating spray, which they attributed to vaporization cooling that contracts the spray.

Using the non-vaporizing and vaporizing data coupled with a simplified model for a fuel jet, Naber and Siebers developed an analytical model describing spray penetration based on conservation of mass and momentum for a steady fuel injection rate into a developing spray control volume. For simplicity, the velocity and mass distributions in the model derivation were assumed uniform at any axial distance from the injector, x. They showed that the form of the spray penetration model developed correlated all the spray penetration and spreading angle data acquired [3]. A constant appearing in the model formulation was adjusted to best fit all the penetration data, accounting for the uniform velocity and mass assumption and thus providing a model that accurately predicts spray penetration when using measured spreading angles from the dataset.

Musculus and Kattke [4] recently extended the Naber and Siebers model by incorporating multiple control volumes and the option for a realistic radial distribution of fuel mass. It will be described in more detail here because we extensively use in it in the following discussions. Figure 1 shows a schematic of the model. By using multiple control volumes, this model allows prediction of penetration and mixing for variable rates of injection, and after the end of injection [4,5]. Spreading angles are still required as inputs to the model. The mass radial profiles within the spray are given by Eq. (1),

$$\frac{\overline{\chi}_f}{\overline{\chi}_{f,c}} = \left(1-\xi^{\alpha}\right)^2 \qquad (1)$$

where $\overline{\chi}_f$ is the turbulent mean fuel liquid volume fraction, the subscript c denotes the value on the jet centerline, and $\xi = r/R$ is the ratio of the radial coordinate r to the jet width, where the jet width is given by $R=\tan(\theta/2)x'$, and θ is the full spreading angle of the spray. As indicated in Fig. 1, the velocity radial profile has the same distribution as the mass profile given by Eq. (1). The exponent α in Eq. (1) is set to a value of 1.5 shortly downstream of the nozzle. This is the recommend value for a fully developed profile [6], which produces a radial profile resembling a Gaussian error function as depicted in Fig. 1. Note that the spreading angle input used is for the very outer edge of the spray R where fuel mass is zero, which may be difficult to locate experimentally. However, other definitions for spray spreading angle are possible because of the well-defined spray radial distribution. For example, if one uses a full-width at half-maximum criteria (FWHM) for the spreading angle, this FWHM spreading angle is approximately 45% of the full angle θ, as prescribed by the radial distribution given by Eq. (1).

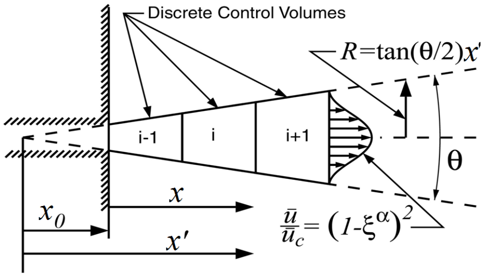

Figure 1: One-dimensional discrete control volume transient diesel jet model of Musculus and Kattke [4].

The radial profile given by Eq. (1) represents the fuel liquid volume fraction with no explicit consideration of fuel evaporation. In addition, the model assumes no velocity slip between injected fuel and entrained gases. Accordingly, momentum transfer between fuel droplets and entrained gas is assumed to be perfectly complete and the local fuel-ambient mixture is independent of whether there are droplets or vaporized fuel. Essentially, droplet size has no effect and there is no difference between this "spray" model and that of a hypothetical gas jet with the same momentum and mass flow rate. The local fuel-ambient mass ratio F/A can therefore be related to $\overline{\chi}_f$ as

$$\frac{F}{A}=\frac{\rho_f \cdot \overline{\chi}_f}{\rho_a \cdot (1-\overline{\chi}_f)} \qquad (2)$$

where ρ_f and ρ_a are the fuel and ambient densities, respectively. The mixture fraction Z, which is equivalent to the fuel mass fraction Y_f if the system is inert, is then

$$Z = Y_f = \frac{F/A}{(F/A+1)} \qquad (3).$$

The model therefore provides a prediction of the local mixture fraction at any position within the spray, dependent upon model inputs such as the full spreading angle θ, ρ_f, and ρ_a, and the assumed radial fuel concentration profile shape. In addition, users must also specify the nozzle area contraction coefficient C_a, and discharge coefficient C_d, to provide specification for both the momentum and mass flow rates of the spray [3-4]. These nozzle coefficients typically must be measured experimentally [3,7-10].

Simplified spray-mixing models similar to the Naber/Siebers or Musculus/Kattke models offer a highly accessible and straightforward method to quantify spray mixing. These models are widely used as tools to aid the interpretation of spray combustion measurements, including estimation of spray mixing to determine liquid-phase penetration length [8] or soot formation trends. These simplified models are also used firsthand to guide spray models within more detailed CFD applications [11,12].

While simplified spray or jet mixing models have been developed, such as the Musculus/Kattke model described above, or the even simpler Naber/Siebers model, their representation of mixing has not been validated against experimental data that include direct measurement of mixing in a fuel jet at diesel conditions. Such comparisons would also offer an opportunity to better "calibrate" these simplified models. The major shortcoming for such comparisons is that quantitative measurement of mixture fraction at high temperature and pressure conditions representative of a diesel is hindered by many experimental difficulties.

The experimental difficulties result from both spray and diagnostics sources. The dense liquid portion of the spray near the nozzle is inaccessible to quantitative optical diagnostics. Downstream of the dense liquid region, laser-based diagnostics for fuel-oxidizer mixing that have been attempted in evaporating diesel sprays include Raman scattering [13-14], laser-induced fluorescence/exciplex fluorescence (LIF/LIEF) [15-17,21], Mie scattering [18-19], and Rayleigh scattering [20-23]. Each technique has its own advantages and disadvantages. For example, elastic scattering techniques like Mie and Rayleigh suffer due to interference from scatterers other than the probed species and Raman scattering is limited by low signal strength and poor spatial resolution (usually 1-D instead of 2-D). In the case of LIF/LIEF techniques, elastic scattering interferences are not as serious, but the fluorescence yield is generally a function of temperature, pressure, and ambient gas composition, making quantitative measurement of transient mixing processes at engine conditions difficult. Exciplex fluorescence has not proven quantitative for liquid concentration [15-17], forcing any attempt at quantification to the fully vaporized "jet" region, rather than the liquid spray region. Also, the injector nozzle coefficients or global parameters such as the liquid spray (or vaporized jet) spreading angle and penetration rate typically have not been reported along with mixing measurements in these studies, making evaluation against a spray mixing model difficult. To date, none of the mixing data from Refs. [13-23] has been used to explore the validity of mixing models like that shown in Fig. 1. Data from Ref. [23], available to download from the Engine Combustion Network [24], was recently used for comparison to various CFD (grid-resolved) spray models [25].

In addition to these experimental challenges for making detailed spray mixing measurements at diesel conditions, many widely used techniques for measuring a primary spray global parameter, the spray spreading angle, are not fully quantitative or easily reproduced. For example, schlieren techniques used for measuring the jet vapor boundary are not quantitatively relatable to the actual mixture fraction at the vapor boundary. This problem is especially difficult when the ambient gas surrounding the spray is at high temperature and pressure. Non-uniformities in ambient gas temperature create refractive index gradients that appear in the "background" of schlieren imaging [1,3,26], making it difficult to determine the boundary between fuel vapor and unmixed ambient gas. Moreover, increasing the ambient gas pressure (or density) intensifies the refractive index gradients as these gradients scale directly with density. The schlieren sensitivity to refractive index gradients can be adjusted optically [27] but this may reduce the ability for detection of the very edge of the spray. Ultimately, it is unknown what mixture fraction corresponds to the jet “border” apparent from variations in the schlieren intensities. As will be shown, however, this challenge is less of on an issue for detecting the leading edge of the penetrating spray penetration, where the spray border is marked by very sharp gradients and is more easily observed and measured.

Yet another complication is that researchers may not make the distinction between the liquid-phase “spray” width or penetration, compared to those of the vapor-phase “jet” at high-temperature, vaporizing conditions. For example, Mie-scattering may be used to measure the liquid-phase spray angle and penetration, which is expected to be different than that of the vapor. Since spray (or jet) models depend upon the spreading angle derived from these boundaries to determine spray breakup, or the amount of ambient gas entrained into the spray, their calibration is suspect without knowledge of the mixture fraction (or fuel-ambient ratio) that corresponds to a particular spreading angle.

OBJECTIVES

Our objectives are to quantitatively measure fuel vapor concentration in evaporating diesel sprays, and to use these data for the following:

- To identify the mixture fraction at the edge of the jet that corresponds to the spreading angle detected by schlieren imaging. We will specifically address complications associated with different schlieren imaging setups and different ambient densities.
- To evaluate the mixing prediction accuracy of the Musculus/Kattke model depicted in Fig. 1, and the Naber/Siebers model, as well as assumptions employed in deriving these models. We will use measured "global" parameters such as the spreading angle and penetration rate, along with measurements of the nozzle flow coefficients as inputs to the model. We will compare model predictions and mixing measurements for a range of ambient densities, fuels, nozzle sizes, and nozzle shapes, to address the robustness of the model at various conditions.

The comparisons will provide new insights into diesel sprays, validate the general structure of the models, elucidate the challenges with making both global measurements of spray mixing (*i.e.*, the spreading angle), as well as spatial resolved measurements of fuel concentration, and point out several spray development issues that remain to be resolved, especially relative to the models.

EXPERIMENTAL APPARATUS

COMBUSTION VESSEL

Experiments were performed in a constant-volume combustion vessel under simulated engine conditions. The combustion chamber is cubical, measuring 108 mm on each side. Figure 2 shows the fuel injector is mounted at the center of a metal side-port such that the diesel spray is directed into the center of the chamber. Windows located in three other ports of the combustion vessel permit line-of-sight and orthogonal optical access to the injected fuel jet. The optical diagnostic setups will be discussed later. Further details about the combustion chamber geometry and operation may be found in [24].

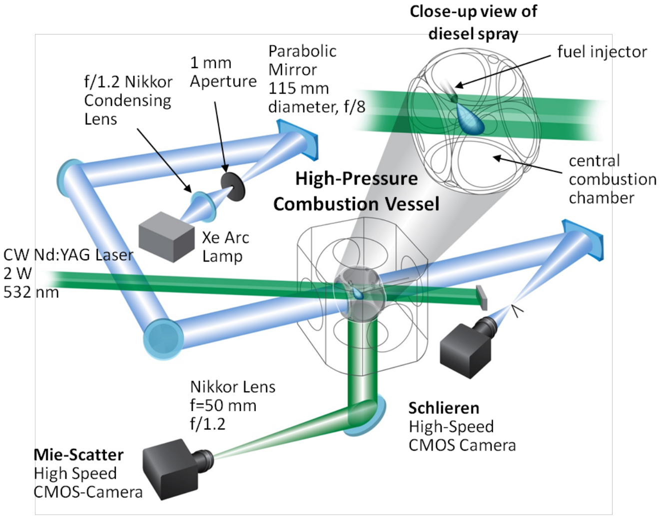

Figure 2: Combustion vessel and high-speed imaging setup (not to scale).

Diesel conditions are simulated by using a premixed, combustible-gases mixture, which is spark-ignited to create a high-temperature, high-pressure environment in the vessel. Following the premixed combustion, the combustion products cool over a relatively long time (~1-3 s) due to heat transfer to the vessel walls and the vessel pressure slowly decreases. When the desired pressure and temperature are reached, the diesel fuel injector is triggered and fuel injection occurs.

The temperature, density, and composition of the ambient gas in the vessel at the time of diesel fuel injection can be varied widely with this simulation procedure. The conditions of the ambient gas at the start of injection are determined by the initial mass and composition of gas within the vessel and the pressure at the time of fuel injection. All Rayleigh and schlieren imaging experiments were performed in an inert environment of 0% O_2, to evaluate the effects of mixing and spray vaporization without the complication of combustion. Table 1 shows the ambient gas composition and range of conditions that were evaluated in this study, which included several different ambient gas densities and temperatures. Temperature measurements were performed by fine-wire thermometry to establish a relationship between pressure and the temperature during the cool down. The gas temperature prior to injection was uniform to within 1% along the axial direction [28].

Table 1. Ambient gas conditions for this study.

%vol O_2	0.00
%vol CO_2	6.52
%vol N_2	89.71
%vol H_2O	3.77
Mol. Weight MW	28.68
Ambient temperature range	900 – 1400 K
Ambient density range	7.6 – 22.8 kg/m^3
Vessel pressure	3.1 - 6.0 MPa

INJECTION EQUIPMENT

Two different common-rail injectors were used in this study, each with a single-spray,axially-drilled, nozzle. The first is the same injection system that was used in our facility from 1998 [7] to 2007 [23]. The fuel injector was a prototype, electronically controlled, common-rail, solenoid-activated injector designed by Detroit Diesel Corporation. Table 2 shows the specifications for the nozzle used in this study (see DDC). The 0.100 mm orifice is sharp-edged, non-hydroground and designed without taper from the inlet to the exit of the nozzle ($K = (d_i - d_o)/10 \approx 0$, units in μm). The second injector is a Bosch second-generationcommon-rail injector (CRIP 2.4).

This nozzle has a convergent(K = 1.5), hydro-ground orifice (KS1.5/86specification by Bosch) and is a mini-sac type with a sac volume of 0.2 mm^3. This injector is now being used for the "Spray A" condition data set of the Engine Combustion Network [24].

Table 2.Injector conditions. Two different injectors were used, with injection pressure and fuel variation.

Inject.	Orifice dia. [mm]	C_d	C_a	K	Fuel	Fuel T^* [K]	P_{inj} [MPa]
DDC	0.100	0.80§	0.86§	0	C7	373	154
Bosch	0.090	0.86	0.95	1.5	C12	363	150
Bosch	0.090	0.86	0.95	1.5	C12	363	100
Bosch	0.090	0.86	0.95	1.5	C12	363	50
Bosch	0.090	0.86†	0.95†	1.5	C7	363	150

§Measured for diesel fuel at 300 K [7].

† assumed to be the same as that measured for n-dodecane

*Calculated fuel density at this temperature and at 1 atm: n-heptane (C7,373 K), 613 kg/m^3; n-dodecane (C12, 363 K), 699 kg/m^3; n-heptane (C7,363 K), 623 kg/m^3

Figure 3 presents rate-of-injection (ROI) measurements that correspond to the injectors used in the study. ROI measurements were performed using a force sensor, and cumulative mass measurements, with the injector installed in the spray chamber. The method was similar to that described in [8]. The injection profiles for either injector have a very rapid start and end of injection, with a steady period in between, forming a top-hat profile. For the 0.100-mm nozzle (DDC injector), we have used the ROI profile measured for this nozzle at a similar condition using diesel fuel, and then applied an appropriate scale factor for n-heptane fuel, which has a lower fuel density. This is necessary because no ROI measurements were made with n-heptane fuel. The ROI measurements for the 0.090-mm nozzle (Bosch injector) are at the stated conditions.

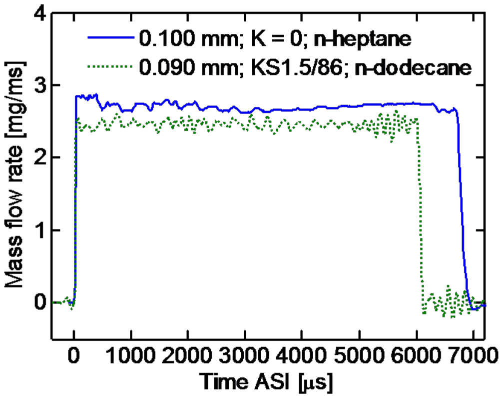

Figure 3: Mass flow rate of injection with 150 MPa fuel injection pressure and 0.1 MPa ambient pressure. The 0.100-mm flow rate is scaled for n-heptane fuel.

A steady fuel injection rate was used to the advantage of Naber and Siebers [3] when developing a model for spray penetration. Their model requires a steady fuel injection rate, and predicts only a steady-state mixture distribution. It should not be used for variable rates of injection. As noted in the Introduction, the Musculus/Kattke [4] model allows variable rates of injection, so an injector that has a ramp-shaped ROI can be evaluated. However, since either injector in this study produces a top-hat ROI with a steady fuel injection rate, we can use penetration or mixing solutions from either the Naber/Siebers model or Musculus/Kattke model. In fact, analytical solutions for penetration and mixing are possible for the Musculus/Kattke model with a steady fuel injection rate, which are provided in Appendix A. The finite-volume solution depicted in Fig. 1 matches the steady fuel injection solution, indicating accurate numerical treatment [4], but it is unnecessary to use the finite-volume approach if the flow is steady. Accordingly, the steady solutions for penetration and mixing given in Appendix A will be used for comparison to experimental results.

The discharge (C_d) and area contraction (C_a) coefficients for the injectors/orifices are shown in Table 2. The orifice coefficients were determined from long-injection events, where the flow is relatively steady, similar to those shown in Fig. 2. Note that the shaped hydroground orifice (0.090-mm) has higher flow coefficients, as expected, compared to the non-hydroground orifice. While the ROI for the 0.090-mm is expected to be lower than the 0.100-mm orifice, the measured flow rate is only slightly lower because of higher flow coefficients.

OPTICAL DIAGNOSTICS

High-speed imaging systems were utilized to simultaneously track the liquid and vapor phases of the spray. Rayleigh-scatter imaging was used for a quantitative measurement of mixing in the vapor-phase region. The setup for these diagnostics is discussed below.

MIE-SCATTER

Scattered light from fuel-spray liquid droplets was imaged using a high-speed CMOS camera and a continuous-wave laser. As shown in Fig. 2, a schlieren system was operated simultaneously using a second high-speed CMOS camera, similar to the setup reported in [26]. The time-resolved pair of schlieren and Mie-scatter images identifies the instantaneous position of both the vapor and liquid phases of the fuel spray, respectively. For clarity, throughout the paper we will refer to the liquid-phase region as the "spray" region and the vapor-phase region as the "jet" region.

The continuous-wave laser source was formed into a volume to illuminate the liquid-phase region of the spray. A volume-illumination method, rather than a laser sheet, was utilized to ensure that all droplets spreading from the nozzle were illuminated to identify the maximum axial and radial distances of any liquid-phase fuel. The input beam was directed at a slight angle to avoid interference with the schlieren setup. A high-speed CMOS camera, fitted with a 532-nm bandpass filter (10-nm FWHM) and a 50-mm focal length f/1.2 lens, was used to image Mie-scattered light at a near-right angle to the laser source.

SCHLIEREN

Schlieren imaging was performed simultaneously using a second lighting and imaging arrangement. Light from a mercury-xenon arc lamp was collimated to pass through the combustion vessel. The collimated beam was then re-focused before entering a high-speed CMOS camera equipped with a lens and a 532-nm 0°-incidence laser mirror to block the light elastically scattered by spray droplets.

Previous studies utilized several different schlieren stops at the collection focal point shown in Fig. 2, including a knife edge, aperture (bright-field), cutoff disk (dark-field), or no stop [26]. The sensitivity of the system to refractive index gradients can be adjusted by the use of different cutoffs [27]. However, gradients of refractive index caused by heat transfer to the cooler vessel wall, which forms temperature gradients in boundary layers near the walls, create schlieren effects that appear in the background of the images [28]. Note that potential disturbances are possible at two window-ambient interfaces, along with an 108-mm path (the vessel dimensions) through high-temperature ambient gases. To illustrate this effect, we show a raw schlieren image with a computer-algorithm-determined jet boundary in Fig. 4. The disturbances outside of the jet in Fig. 4 show significant light-dark fluctuations with a relatively small length scale. Inside of the jet, the texture of the image appears smoother. The significant schlieren disturbances that persist outside of the jet clearly make it difficult to determine the true vapor boundary, thereby causing uncertainty in the jet penetration rate and spreading angle. If the schlieren sensitivity is too high, the background disturbances of the ambient will appear too prominent in the images, making image processing for detection of the jet boundary impossible. On the other hand, if the schlieren sensitivity is too low, the vapor border of the jet may not be detected. In addition, these schlieren disturbances change with ambient density. Therefore, several different schlieren setups were investigated.

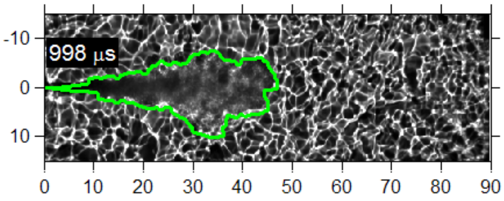

Figure 4: Example schlieren image with processed vapor boundary shown in green. High-sensitivity schlieren setup, 22.8 kg/m^3, 6 MPa.

Table 3 shows the imaging parameters for a low-sensitivity setup and a high-sensitivity setup. In either setup, we found adequate sensitivity to refractive index gradients when using no schlieren stop other than the camera aperture. The high-sensitivity setup utilizes a camera lens with 105-mm focal length and set for infinite focus. This setup provides higher pixel resolution at the expense of a slower framing frequency. The low-sensitivity setup uses a 50-mm focal length lens set for 3 m focus, rather than infinite focus. As will be shown, de-focusing the lens and using lower pixel resolution tends to smear schlieren disturbances from the ambient, making image processing easier. The lower pixel resolution also allows faster camera framing rates to capture the penetration of the jet with higher time resolution.

Table 3.High-speed CMOS camera schlieren imaging setup.

	high-sensitivity setup	lower-sensitivity setup
Lens focal length	105 mm	50 mm
Lens focal setting	∞	3 m
Lens f/#	2.8	1.2
Pixel resolution	512 x 256	256 x 128
Spatial resolution	5.4 pixel/mm	2.7 pixel/mm
Frame period	66.5 µs	21.2 µs
Exp. period	3 µs	2 µs

In addition to schlieren imaging setup variation, changes to background schlieren disturbances were accomplished by adjusting the vessel mixing fan speed, or by turning the fan completely off. Adjustments to the fan speed tend to change the length scale of the structures in the background [26], potentially making it easier to detect the jet.

RAYLEIGH-SCATTER IMAGING

Quantitative mixing measurements in a vaporizing fuel sprays were obtained using Rayleigh-scatter imaging. Most of the experimental approach to Rayleigh-scatter imaging in our facility is covered in Ref. [23]. As only a few modifications to this setup were made for this study, an abbreviated summary of the experimental approach is included here with special attention to the new setup. By avoiding scatter from liquid-phase droplets, Rayleigh-scatter imaging provides a measurement of the mixture fraction within the vaporized portion of the fuel spray.

Optical setup

The laser light source for Rayleigh-scatter imaging was the second harmonic of an Nd:YAG laser (532 nm) with pulse energy of 150 mJ and pulse duration of 7 ns. The laser beam was formed into a collimated planar sheet 40 mm wide and 300 µm thick and passed through the fuel jet center. The laser sheet spanned axial distances from approximately 17 mm to 57 mm. The signal was filtered with a 532-nm narrow band filter (10 nm FWHM) and imaged using a high-quantum-efficiency, back-illuminated CCD camera (PIXIS 1024B). Two different imaging setups were utilized, with a comparison of the two setups shown in Table 4. The setup changed between experiments using the DDC injector [23] and newer experiments using the Bosch injector. A more detailed discussion of the theory of Rayleigh scattering and the setup changes is included in Appendix B.

Table 4. Camera and lens configurations for Rayleigh-scatter imaging.

Injector orifice setup	0.100-mm [23]	0.090-mm
PIXIS Camera	1024B-UV	1024B
Q.E. at 532 nm	66%	95%
Gain	1 [cts/e-]	0.25 [cts/e-]
Lens focal length	105 mm	85 mm
Lens f/#	f/1.8	f/1.4
Close-up	10 mm extens.	500 D lens
Pixel resolution	20.09 pix/mm	14.06 pix/mm
Laser trans. windows	Sapphire	Fused-silica slits

Liquid penetration length control

Mie-scatter interferences from liquid-phase droplets can be avoided by positioning the laser sheet downstream of the maximum liquid-phase penetration distance, or the liquid length (see Fig. B1 in Appendix B). However, the liquid length changes depending upon the fuel and operating condition [8]. For example, variation of ambient density is one of the primary objectives of this study, and, as shown in Fig. 5, the liquid length tends to increase with decreasing ambient density. Therefore, avoiding interference from liquid droplets by the Rayleigh diagnostic becomes more problematic. One potential solution is to change the laser sheet position for each density, i.e., to move the laser sheet downstream at lower density. However, this limits the range of data that can be used for calibration of the jet mixing model and it requires a new, repeatable setup for each condition. Another approach is to raise the ambient temperature when decreasing ambient density to prevent liquid droplets from entering the laser sheet interrogation region. For example, Fig. 5 shows that in order to maintain an n-dodecane liquid length of approximately 11 mm, far enough away from the laser sheet at 17 mm, the ambient temperature must be increased from 900 K at 22.8 kg/m^3, to above 1400 K at 7.6 kg/m^3.

If droplets mix perfectly with the ambient (no velocity slip), the momentum transfer between the injected fuel and the ambient gases depends only upon ambient density, rather than ambient temperature. In fact, there is no temperature input in the spray mixing model of Musculus [4] or Naber and Siebers [3]. Accordingly, we adopted the approach of increasing ambient temperature when decreasing ambient density to keep the liquid length essentially constant.

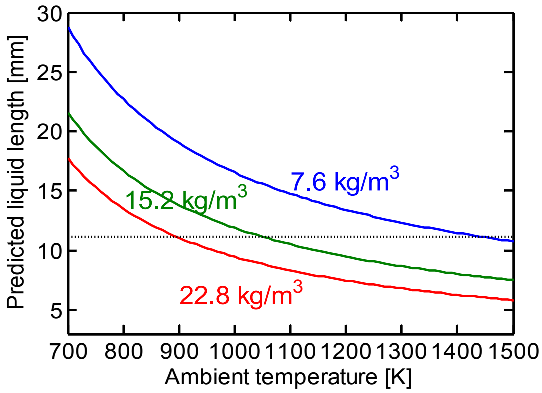

Figure 5: Predicted liquid penetration lengths for n-dodecane as a function of ambient density. Model of Siebers [8].

Increasing ambient temperature can adversely affect the Rayleigh-scatter signal, however, if the elevated temperature causes the fuel molecules to decompose. Analysis in Appendix B shows that fuel decomposition is a concern when the ambient gas temperature is 1400 K. Despite the likelihood for fuel decomposition when the ambient temperature is 1400 K, we performed Rayleigh scattering experiments at this condition to address the effect of lower ambient density (7.6 kg/m^3) on mixing. Although fuel decomposition can significantly reduce signal (limiting case is a factor of 2.4, see Appendix B), the signal is not completely eliminated and Rayleigh scattering could be used to assess such things as the vapor boundary of the jet in connection to that determined by schlieren imaging, for example. We will return to this issue and address fuel-decomposition along with its potential influence on our quantitative mixing measurements later in the results.

Uncertainty analysis

As the purpose of this paper is to compare experimental mixing measurements to the jet mixing model predictions, the ensemble-average of multiple injections will be provided. The uncertainty for the mean of a dataset depends upon the number of data points, the fluctuation (standard deviation), and any bias errors that remain uncorrected. We follow the standard uncertainty analysis method outlined by Moffat [32], where these error terms are combined and uncertainties expressed to a 95% confidence level.

Systematic errors and uncertainties in the Rayleigh diagnostic have been described in Ref. [23] or in Appendix B, along with methods to minimize these errors. However, a major source of uncertainty for this dataset is the limited number of Rayleigh-image realizations at a particular condition. At most, only 40 images were used to calculate the ensemble average, and in some cases, as few as 20. The number of obtained images is limited by the low repetition rate of injection events for the facility, coupled with the fact that many images were not processed if particle contamination was too severe. A higher uncertainty results when there are few images. We will be careful to present experimental results including uncertainties to qualify how well results match the jet mixing model.

RESULTS

The jet vapor boundary detection by high-speed schlieren imaging, and the derived jet penetration and spreading angle are shown first. We compare these measurements to penetration predictions by the simplified spray mixing model (Fig. 1) and provide an initial assessment of methodology for calibration of these models from global spray measurements. We then compare the measured spreading angle to that determined by Rayleigh-scatter imaging by quantitative comparison of Rayleigh mixing measurements and jet model predictions.

VAPOR BOUNDARY

Examples of schlieren images taken at 3 ms after start of injection (ASI) are shown in Figs. 6-8 for a range of conditions. The schlieren images are shown with computer-processed boundaries in green to indicate the vapor border of the jet. The boundary is determined by analysis of the difference between successive images (I_n - I_{n-1}), which are shown at the bottom of each image pair (raw schlieren at top, I_n). This method for image processing and display attempts to remove schlieren effects that exist in the ambient gases as discussed above. The significance of these background disturbances is clearly manifest. Figure 6 shows how these background disturbances can be changed by switching between an optical setup with high- (top) or low-sensitivity (bottom). Figure 8 shows that the disturbances increase with increasing ambient density, as expected because gradients of refractive index scale with density. Figure 7 shows that the length scale of these disturbances can be increased by turning the mixing fan for the vessel completely off, which can be useful for determination of whether structures originate from the jet or from the ambient [26].

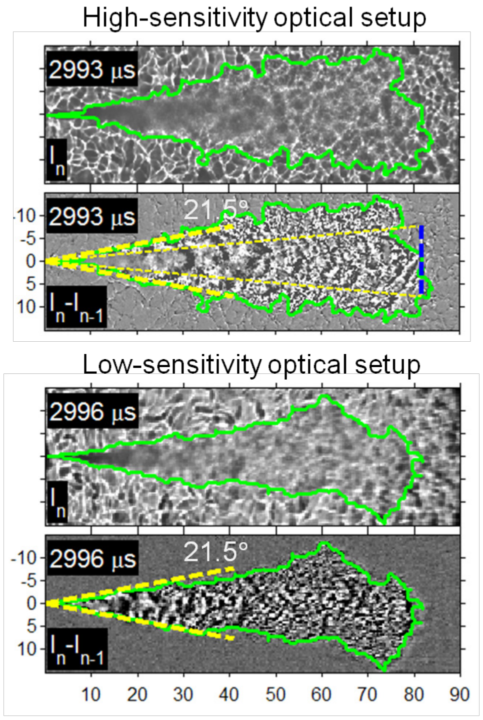

Figure 6: Schlieren imaging with the computed vapor boundary shown in green. Image pairs are shown without (top, I_n) and with (bottom, I_n-I_{n-1}) background correction. Top image pair is for high-sensitivity optical setup (Table 3), bottom for low-sensitivity. Ambient conditions: 900 K, 22.8 kg/m^3, 6.0 MPa. Injector conditions: 0.090-mm orifice, 150 MPa fuel pressure, n-dodecane, 363 K.

The defining boundaries for jet penetration distance and spreading angle, extracted from this vapor boundary, are illustrated in the top image pair of Fig. 6. We have adopted the same definitions used by Naber and Siebers [3]. The jet spreading angle is determined using the portion of the jet that is between the injector and one-half the jet penetration distance to avoid artifacts of the jet head where the jet is not fully developed. The area of the vapor boundary in this upstream region is fit to a triangle having the same area. The angle of this triangle is the instantaneous spreading angle. The steady-state average spreading angle (21.5°) at this condition and optical sensitivity is drawn on the figure with a bold, dashed line extending one-half of the jet penetration distance. Average spreading angles for other conditions and optical setups are included in Table 5.

Table 5. Schlieren measurement or jet model penetration fit of spreading angle, all with 150-154 MPa injection pressure.

Nozzle dia. [mm]	Amb. Density [kg/m^3]	Amb. Temp. [K]	Low-sens. full angle [°]	High-sens. full angle [°]	Penetrat. fit angle [°]
0.100	14.8	1000	-	24.0	23.0
0.090	7.6	1400	16.3	20.2	20.0
0.090	15.2	1100	18.1	21.2	21.5
0.090	22.8	900	18.7	21.5	21.5

The jet penetration distance is obtained using the vapor boundary within the inner half of the spreading angle, as shown by the light dashed lines. The jet penetration distance is defined as the distance along the spray axis where one-half of the pixels across this inner angle have been identified as vaporized fuel. This definition accounts for fluctuations or asymmetry in penetration at the jet head, whether real or artifacts of image processing, to provide a more consistent definition for jet penetration than the maximum vapor boundary. For example, the selected image at the top of Fig. 6 shows longer penetration at the bottom of the jet. The computed penetration distance, shown as a dashed blue line in Fig. 6, gives a better representation of the average jet penetration, including both the top and the bottom of the jet.

The bottom image pair of Fig. 6 shows the change in computed vapor boundary when comparing a low- and high-sensitivity optical setup. The background-corrected image (I_n - I_{n-1}) at the very bottom portrays a convincing impression that the jet border is captured well. The background outside of the jet appears almost completely flat, an improvement compared to the background shown in the high-sensitivity setup where structures persist. However, the jet border appears more narrow with low-sensitivity. To show this comparison, dashed lines are placed on the image for the jet angle calculated with the high-sensitivity setup (21.5°). With this reference, it appears that the jet is slightly more eroded at distances from the injector greater than 30 mm. The calculated spreading angle bears this out. Table 5 shows that the low-sensitivity schlieren setup produced an average spreading angle (from multiple injections) of 18.7°, several degrees smaller than the high-sensitivity setup. This difference in spreading angle may seem slight, but it has a significant impact on the model jet mixing prediction.

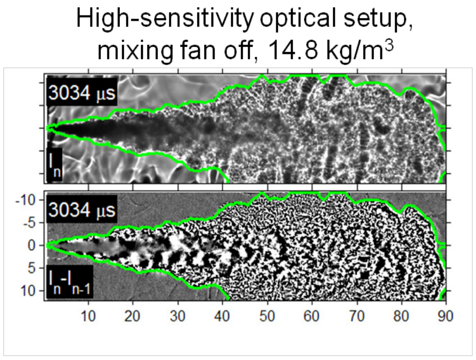
High-sensitivity optical setup, mixing fan off, 14.8 kg/m^3

Figure 7: Schlieren imaging with high-sensitivity optical setup. Ambient conditions: 1000 K, 14.8 kg/m^3, 4.3 MPa. Injector conditions: 0.100-mm orifice, 154 MPa fuel pressure, n-heptane, 373 K.

Schlieren images and vapor boundaries are shown for a different injector and experimental condition in Fig. 7. The high-sensitivity of the optical setup once again provides convincing evidence that the vapor boundary of the jet has been identified quite well. Capturing this vapor boundary was made easier by turning the mixing fan for the vessel off, which lessens the disturbances in the background. In addition, the ambient density is lower compared to Fig. 6, also lessening the effect of schlieren disturbances in the background. Because of the lower ambient density, as well as the larger nozzle orifice size, the jet penetrates farther at the same time ASI compared to that of Fig. 6. Table 5 shows that the spreading angle for this 0.100-mm non-hydroground orifice is 24.0°, compared to 21.2° for the 0.090-mm hydroground orifice at a similar ambient density (in the same optical sensitivity). A smaller spreading angle for sprays issuing from hydroground orifices is consistent with observations in the literature [33-34].

More effects of ambient density upon the schlieren imaging and derived spreading angle are demonstrated in Fig. 8, where results for the low-sensitivity setup are given at lower ambient densities. Once again, the trend of less severe schlieren disturbances in the background continues with reduced densities. The spray also penetrates more quickly across the chamber at low ambient density. The 7.6-kg/m^3 spray has already impinged upon the back wall at 3 ms ASI, while the 15.2-kg/m^3 spray has not reached 90 mm yet. Spreading angles for the same injector orifice, given in Table 5, show that spreading angle increases with increasing ambient density. Past studies have shown this same result [e.g., 3,7,34], though with varying dependency upon ambient density. The spreading angle trend with respect to density is demonstrated with either low- or high-sensitivity schlieren setup (Table 5), but the low-sensitivity spreading angles continue to be several degrees smaller.

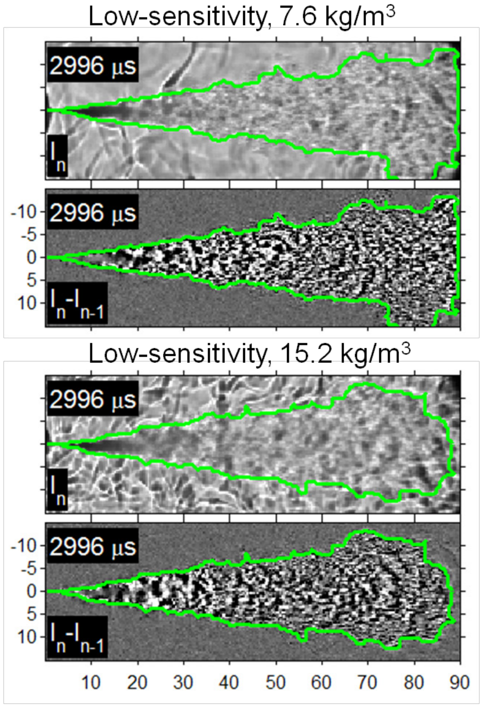

Figure 8: Schlieren imaging with low-sensitivity optical setup at two different ambient densities. (top) 1400 K, 7.6 kg/m^3, 3.1 MPa (bottom) 1100 K, 15.2 kg/m^3, 4.9 MPa. Injector conditions: 0.090-mm orifice, 150 MPa fuel pressure, n-dodecane, 363 K.

Although the derived spreading angle retains sensitivity to the schlieren optical setup, Fig. 9 shows that the measured spray penetration is virtually the same regardless of the setup. The ensemble-averaged penetration of five injections is shown with either high-or low-sensitivity. The measured penetration is the same within the uncertainty of the measurement. Figure 9 also shows model predictions of penetration using the Musculus/Kattke spray model with inputs for spreading angle based on the schlieren measurement. The model predictions show excellent agreement with experimental results when using the high-sensitivity spreading angle, 21.5°, while a smaller spreading angle (18.7°) gives penetration rates that are too high.

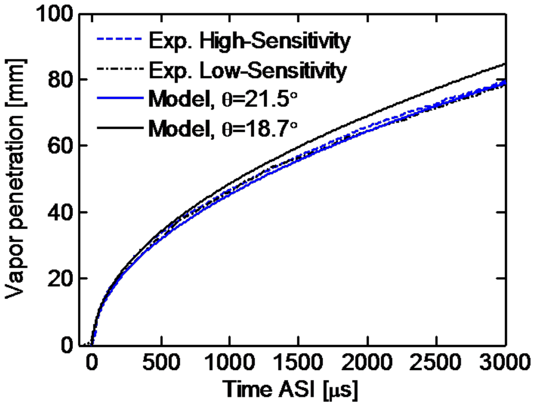

Figure 9: Measured spray vapor penetration with high- and low-sensitivity schlieren setup, along with modeled spray penetration using the measured spreading angles for these setups (see Table 5). Conditions the same as Fig. 6.

There are two important implications from these observations. First, the better schlieren setup for detection of the vapor boundary appears to be that with high-sensitivity. Although schlieren artifacts become more prominent in the ambient background, reverting to a less sensitive setup can result in undetected vaporized fuel. Second, when the schlieren sensitivity is high enough to measure the very outer boundary of the jet and its corresponding spreading angle, this same spreading angle provides accurate predictions of the jet penetration. Therefore, the two measurements are self-consistent and point to a single jet-mixing model input for spray dispersion to match both spreading angle and penetration. Intuitively, this self-consistency should be expected because the penetration is dependent upon the total entrainment and mixing, with the spreading angle being proportional to the rate of ambient entrainment.

Figures 10 to 12 show measured experimental jet penetration and model predictions for a wider set of conditions, including fuel injection pressure variation. For these figures, the model input spreading angle was adjusted to give a best fit to the penetration data rather than relying upon the measured spreading angle. These model spreading angle are included in Table 5, which shows that the best-fit model spreading angle is within 1° of the spreading angle measured by high-sensitivity schlieren. This result supports the idea that the input model angle required to match the measured penetration will be closest to that measured with high-sensitivity schlieren, as was demonstrated in Fig. 9. Figure 12 also shows that the same spreading angle (21.5°) matches the penetration rate for a wide range of fuel injection pressures, indicating that spreading angle does not change with fuel injection pressure [3,35]. An implication from this result is that local fuel-ambient mixture (radial or axial position) also does not change with fuel injection pressure [7,8].

The observations above suggest that the measured jet penetration alone can be used to determine the appropriate model input for spreading angle. The jet penetration is much easier, and more consistent to measure than spreading angle. Figure 9 showed that the measured jet penetration has a low dependence upon a particular schlieren setup, which is definitely not the case for spreading angle measurement. One can easily imagine spreading angle variability from one schlieren setup to the next, based on both differences in optical sensitivity as well as image processing. These observations support the idea that the jet penetration measured by schlieren, rather than the spreading angle, is the best approach to assess the amount of ambient entrainment into the jet. This level of ambient entrainment can be captured in the model by adjusting the spreading angle to match the jet penetration.

Overall, these results suggest a new approach to the calibration of our jet mixing model. Over a wide range of conditions, our results indicate that the ambient entrainment into the model should be based on measured spray penetration, yielding close agreement with the spreading angle and penetration extracted from high-sensitivity schlieren measurements. Once again, we find that it is much easier to use the measured spray penetration, coupled with model predictions for spray penetration, to determine the spreading angle for the spray, rather than using less accurate (or repeatable) schlieren measurements of spray angle. Ultimately, the important point is whether or not this methodology produces accurate mixing predictions. We will explore this question in the following sections.

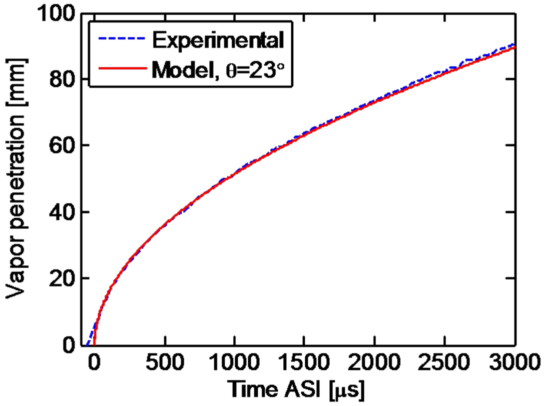

Figure 10: Measured spray vapor penetration and modeled spray penetration using indicated spreading angle. Ambient conditions: 1000 K, 14.8 kg/m^3, 4.3 MPa. Injector conditions: 0.100-mm orifice, 154 MPa fuel pressure, n-heptane, 373 K.

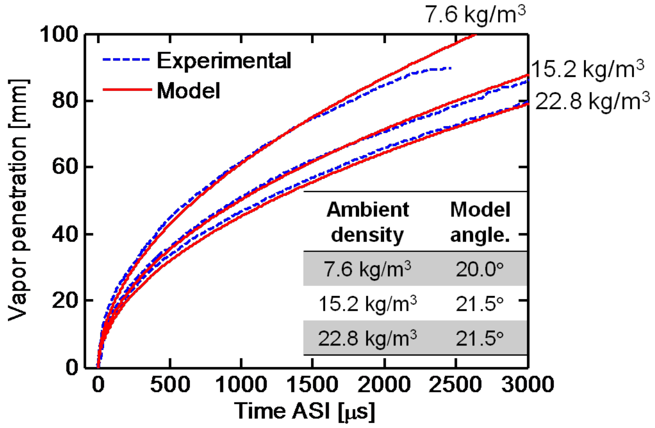

Figure 11: Measured spray vapor penetration and modeled spray penetration using indicated spreading angle. Injector conditions: 0.090-mm orifice, 150 MPa fuel pressure, n-dodecane, 363 K.

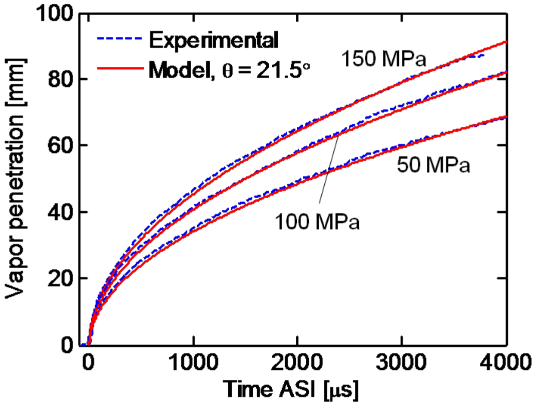

Figure 12: Measured spray vapor penetration as a function of injection pressure, and modeled spray penetration with 21.5°. Ambient conditions: 900 K, 22.8 kg/m^3, 6.0 MPa. Injector conditions: 0.090-mm orifice, n-dodecane, 363 K.

MIXING MEASUREMENTS AND PREDICTIONS

Rayleigh-scatter mixing measurements were obtained at long delays after the start of injection (ASI) to ensure that the spray is steady-state and that transients of the jet head penetration do not affect the measurement region. Image timings ranged from 3.2 – 7 ms ASI depending upon the operating conditions. The spray penetration figures and the schlieren images above give an indication of the time required for the spray to penetrate across the chamber with changes in ambient density (and injection pressure). Thus, earlier imaging times (3.2 ms ASI) were used at low density (7.6 kg/m^3) and high injection pressure (150 MPa) and later times for vice versa. The spray eventually impinges against the back wall, but it forms into a radial wall jet that does not wrap around to the measurement location at the image timing. As a result, the ambient gases remain undisturbed at 50 mm from the injector (extent of laser sheet). See, for example, the schlieren images at 3 ms ASI in Fig. 8, or the Rayleigh image shown in Fig. B1 at 6 ms ASI. Injection durations were also adjusted to ensure that the injection rate was steady-state at the time of image acquisition.

Rayleigh-scatter mixing results are compared to mixing predictions using the Musculus/Kattke model over a wide range of conditions in Figs. 13-19. To illustrate how well the model compares to the experimental results in a meaningful, quantitative manner, we show the axial decay of centerline mixture fraction at the top of each figure and several radial profiles of mixture fraction at a particular axial position at the bottom of each figure. This format is followed for all of these figures. The ensemble-averaged experimental results are shown as blue lines, the model predictions as red lines, and measurement uncertainty 95% confidence intervals are shown as gray fill. If model predictions pass within the gray fill region, they are accurate within the uncertainty of the experimental measurements. As explained in the previous section, jet model predictions are based on inputs for spreading angle that match the measured penetration data, as well as the measured discharge and area-contraction coefficients and fuel density given in Table 2.

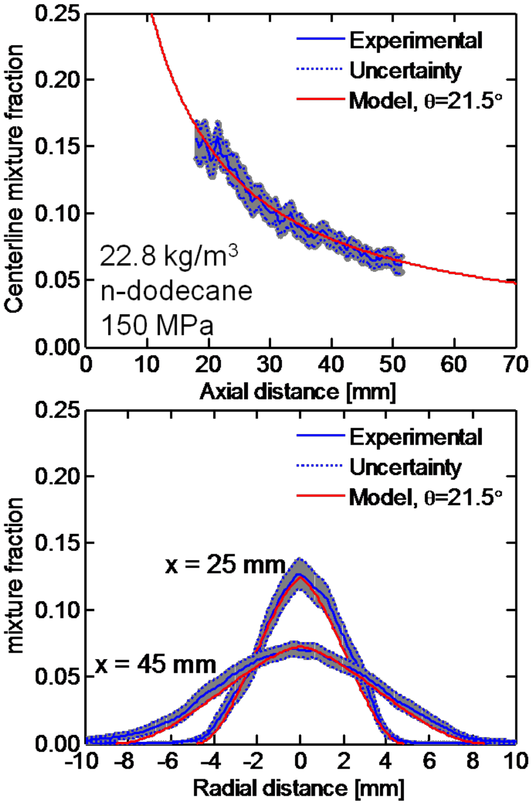

Figure 13: Measured mixture fraction and model predictions at centerline (top) and radial positions (bottom). Ambient conditions: 900 K, 22.8 kg/m^3, 6.0 MPa. Injector conditions: 0.090-mm orifice, 150 MPa, n-dodecane, 363 K.

We begin with Fig. 13, which is for experimental conditions that have been discussed in much detail above (22.8 kg/m^3, 900 K, n-dodecane) and that are the target experimental condition for "Spray A" research of the Engine Combustion Network [24,29]. The figure shows that the model predictions for mixture fraction fall within the experimental uncertainty when using a model input spreading angle of 21.5°. Recall that this spreading angle produces an excellent fit to the measured spray penetration (Fig. 9), and it also corresponds to the measured spreading angle when using high-sensitivity schlieren (Fig. 6). The radial profile for fuel mass distribution for the spray model was described in Eq. (1), which resembles a Gaussian error function. Based upon the closeness of the fit to the experimental data, this radial profile appears justified.

The model spreading angle input used for this radial profile is for the very outer edge of the jet, where the model mixture fraction is zero. The outer edge of the jet is also where the model radial distribution varies somewhat compared to a Gaussian error function. The model profile goes to zero at a radial position where the Gaussian error function is higher, approximately 3% of the centerline value [4]. Therefore, if the actual experimental profile were shaped more like a Gaussian error function, the Musculus/Kattke model would be expected to fall slightly lower than then experiment near the jet edge. Because of the low gradients in mixture fraction and finite experimental uncertainty, however, the exact zero-crossing is difficult to define when using the measured Rayleigh data, so a detailed comparison of the model and experiment is not warranted at the jet outer edge. We can only conclude that the experimental and model mixture-fraction profiles do go to near-zero at a similar radial distance. Since the spreading angle is defined as the radial position where mixture fraction is zero ($Z = 0$), and this spreading angle matches that of high-sensitivity schlieren, the implication is that high-sensitivity schlieren will detect very low mixture fraction/fuel vapor concentration. This certainly seems consistent with high-sensitivity schlieren images shown above (see Fig. 6), where the fuel jet boundary is discernible above disturbances in the ambient background. As discussed previously, however, optical setup and image processing to detect this vapor boundary (near $Z = 0$) with schlieren imaging remains a challenge.

Quantitative mixture fraction distributions from Rayleigh-scattering measurements farther away from the very edges of the jet can enable a more detailed comparison between measured and model spreading angle. For example, defining the spray spreading angle at full-width half-maximum (FWHM) may be preferred because gradients in mixture fraction are more pronounced, and this definition is perhaps more common in the literature for simple gas jets. Analyzing the mixture fraction distributions at 25 mm and 45 mm from the injector shows that the model FWHM for mixture fraction is 4.5 mm and 7.9 mm, respectively, or a 10.0-10.2° angle. This is less than one-half of the angle if spreading angle is defined at $Z = 0$, as is the convention for the model. The measured mixture fraction shows uncertainties that encompass the model predictions at the FWHM position, with the average varying by less than 10% of the model predictions. Ultimately, various definitions for spreading angle are possible, but the end result is a close agreement between experimental and modeling radial distributions. Without quantitative mixing information inside of the jet boundary, as is the case for schlieren measurements, this comparison is not possible.

Another significant finding demonstrated in Fig. 13 is that the spray centerline mixture fraction follows an approximately $1/x$ decay with respect to axial distance, which is the form predicted by the model as demonstrated in Appendix A. The model also predicts radial mixture fraction profiles that are self-similar, meaning that the distribution collapses when normalized by the centerline mixture fraction, and the spray outer radius, R (see Eq. (1)). Based on the closeness of the experimental data to this self-similar model, the conclusion is that mixing in evaporating sprays is indeed self-similar. While this is a well-known result for gas jets, data to support this conclusion has been scarce in evaporating diesel sprays. Previous works using LIF have shown that data collapse when normalized by the jet outer radius [15,17], but measured centerline values do not follow a $1/x$ decay [15,17]. Possible reasons for this discrepancy include measurements that are taken where the fuel jet is not entirely steady (i.e., the head region) [15,17], significant absorption and fluorescence corrections [15], and measurements presented over a narrow range of axial distances (12 mm) [17]. The Rayleigh-scattering imaging results given in Fig. 13 convincingly show a $1/x$ decay for an axial measurement domain spanning more than 30 mm, starting near 20 mm from the injector. The radial distributions are also self-similar within this range of axial distances.

To determine if such findings apply more generally, we will now discuss results from other experimental conditions given in Figs. 13-19. Figures 13-15 demonstrate the effect of fuel injection pressure; Figures 13, 16, and 19, the effect of ambient density; Figure 17, the effect of nozzle size and shape, as well as fuel; and Figure 18, the effect of fuel and ambient density. The major conclusion is that model predictions for mixture fraction nearly fall within experimental uncertainty for all of these conditions. These results further justify the use of a model with the ambient entrainment determined by the measured jet penetration. There is also good agreement for a range of ambient densities, fuels, and nozzle shapes, indicating that the model jet contains the proper physics to predict mixing over this range of parameters. Indirectly, the good agreement between model and experimental mixing results supports the integrity of the experimental mixing measurements by Rayleigh scattering.

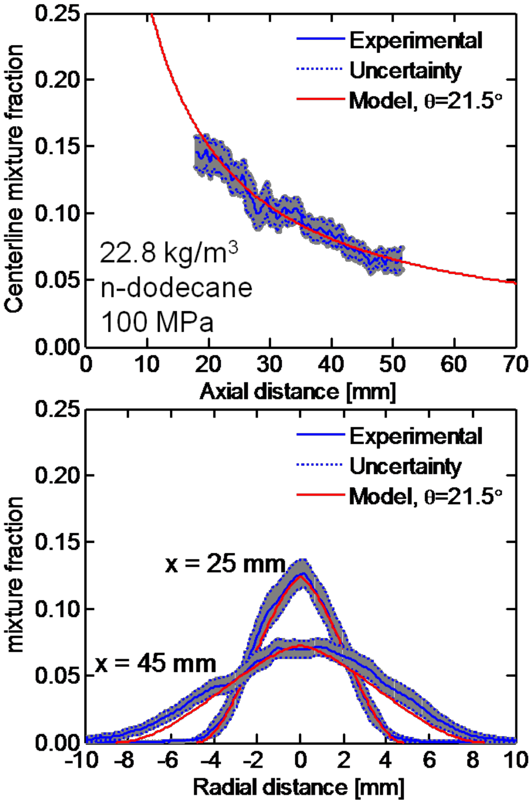

Figure 14: Measured mixture fraction and model predictions at centerline (top) and radial positions (bottom). Ambient conditions: 900 K, 22.8 kg/m^3, 6.0 MPa. Injector conditions: 0.090-mm orifice, 100 MPa fuel pressure, n-dodecane, 363 K.

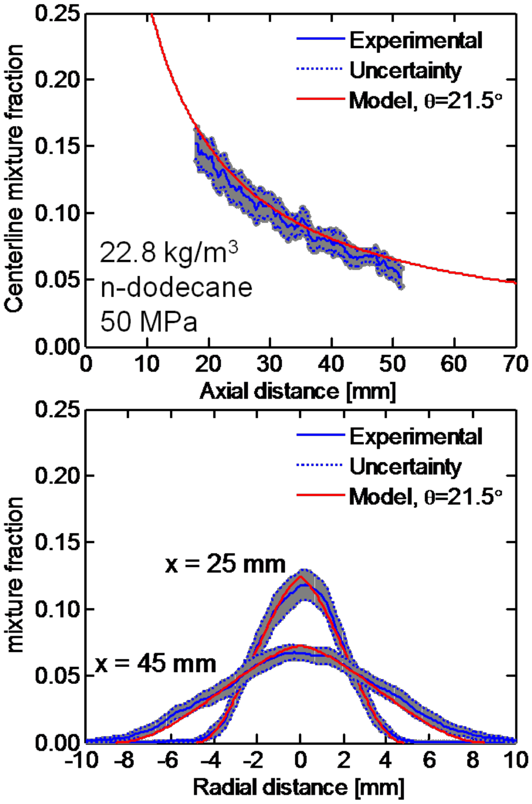

Figure 15: Measured mixture fraction and model predictions at centerline (top) and radial positions (bottom). Ambient conditions: 900 K, 22.8 kg/m^3, 6.0 MPa. Injector conditions: 0.090-mm orifice, 50 MPa fuel pressure, n-dodecane, 363 K.

The measured mixture fraction as a function of injection pressure as given in Figs. 16-18 is an example of the consistency of the data. The model mixing predictions are actually identical in all of these figures because they have the same spreading angle. As was shown in the penetration data of Fig. 12, the same 21.5° spreading angle is justified for each injection pressure. The mixing predictions do not depend upon injection velocity because an increase or decrease in velocity is matched by an increase or decrease in ambient entrainment, a well-known result for gas jet mixing. Since the model predictions are identical and they generally fall within the measurement uncertainty, the conclusion is that there is no measurable difference in mixture fraction with respect to injection pressure. The data also support the observations made above about self-similar mixing in vaporizing sprays. Centerline mixture fraction decays as $1/x$ and the measured radial distributions follow the self-similar model.

The lack of dependence upon injection pressure for spray mixing is supported by several other observations in diesel sprays. First, studies show almost no effect of injection pressure upon the spray spreading angle once the spray has reached steady-state [3,35-37]. Second, the liquid-phase penetration length does not depend upon injection pressure [7] and supporting models for liquid vaporization show that it is controlled by mixing [8]. Third, the flame length for reacting diesel sprays does not depend upon injection pressure, implying similar levels of air entrainment to reach complete combustion at the same axial distance [38].

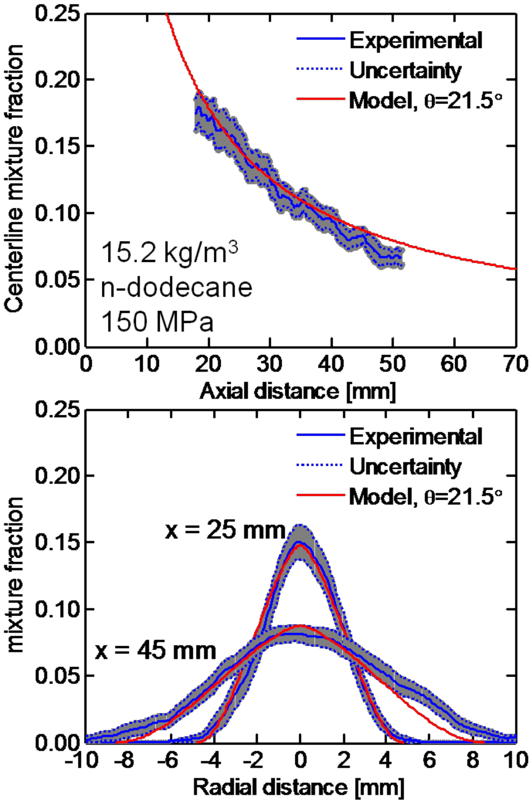

Figure 16: Measured mixture fraction and model predictions at centerline (top) and radial positions (bottom). Ambient conditions: 1100 K, 15.2 kg/m^3, 4.9 MPa. Injector conditions: 0.090-mm orifice, 150 MPa fuel pressure, n-dodecane, 363 K.

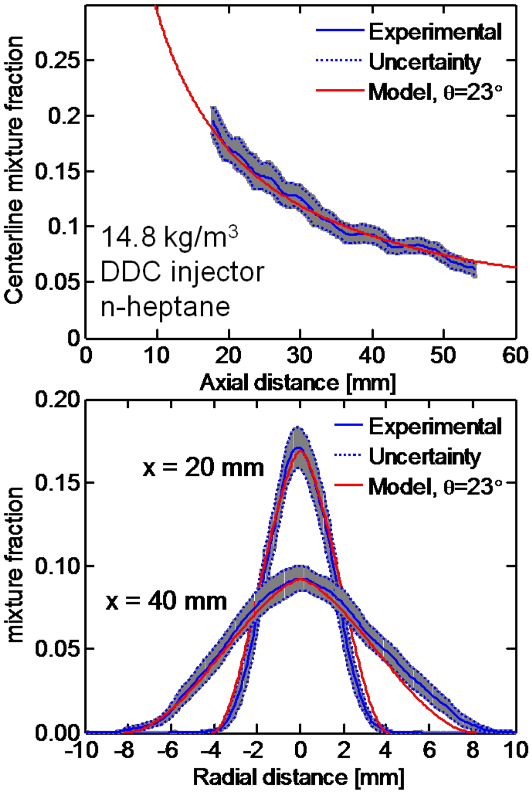

Figure 17: Measured mixture fraction and model predictions at centerline (top) and radial positions (bottom). Ambient conditions: 1000 K, 14.8 kg/m^3, 4.3 MPa. Injector conditions: 0.100-mm orifice, 154 MPa fuel pressure, n-heptane, 373 K.

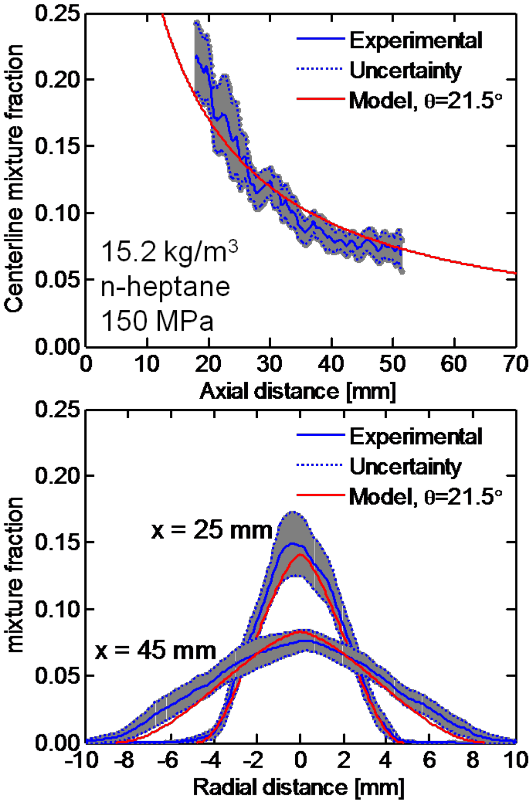

Figure 18: Measured mixture fraction and model predictions at centerline (top) and radial positions (bottom). Ambient conditions: 1100 K, 15.2 kg/m^3, 4.9 MPa. Injector conditions: 0.090-mm orifice, 150 MPa fuel pressure, n-heptane, 363 K.

One experimental condition that does not match model predictions is that with an ambient gas temperature of 1400 K (Fig. 19), but fuel decomposition is the cause in this case. As explained in Appendix B, fuel decomposition is expected when the ambient gas temperature is this high. The expectation is that breakdown of the fuel molecule will cause a reduction in Rayleigh-scattering signal (Table B2), which is the symptom shown in Fig. 19. Experimental mixture fractions fall 30% - 50% lower than modeling predictions. There is no way to account for this lost fuel mass, except by experimental artifact, as the model predictions show wider radial distributions, but also higher fuel mixture fraction. Table 6 shows that complete fuel decomposition to C1 fragments would decrease the Rayleigh signal by a factor of 2.4 for stoichiometric mixtures. The reduction in signal is far less than a factor of 2.4, indicating only partial fuel decomposition. Nevertheless, the Rayleigh signal is no longer quantitative and comparison to model predictions is not warranted. However, later we will discuss several qualitative observations about the spreading angle for this experimental condition as measured by Rayleigh scattering in comparison to schlieren imaging.

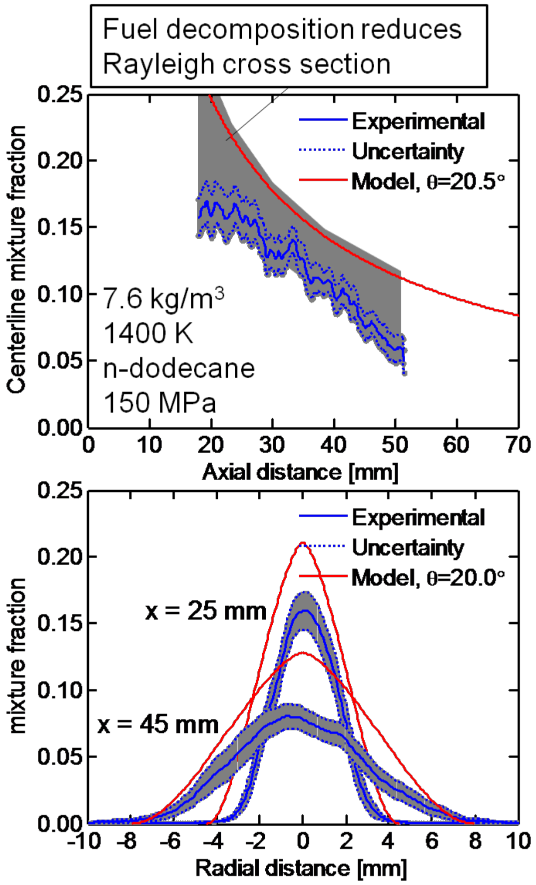

Figure 19: Measured mixture fraction and model predictions at centerline (top) and radial positions (bottom). Ambient conditions: 1400 K, 7.6 kg/m^3, 3.1 MPa. Injector conditions: 0.090-mm orifice, 150 MPa fuel pressure, n-dodecane, 363 K.

With respect to ambient density, Figs. 13, 16, and 18 show that mixture fraction increases with a decrease in the ambient density at a given axial position. Effectively, less ambient mass is entrained into the fuel jet at a given axial position, making the mixture more fuel-rich. The experiment and model capture this trend for a decrease in ambient density by one third (22.8 kg/m^3 to 15.2 kg/m^3). At 15.2 kg/m^3, Fig. 16 does show that model predictions match upstream, but then fall slightly less than the experimental uncertainty band towards the outer radius of the vaporized jet downstream at an axial distance of 45 mm. The trend is also manifest for a different nozzle at a similar density (14.8 kg/m^3) in Fig. 17. One simple explanation for this result is that the experimental spreading angle increases to some extent with axial distance, unlike the assumption in the model.

To check if there is experimental evidence to support an increase in spreading angle at some axial distance and how it depends upon ambient density, we show the full-width half-maximum FWHM of the vaporized jet determined from the Rayleigh-scattering measurements as a function of axial distance in Fig. 20. The experimental FWHM is shown along with a linear fit for each ambient density. (Note that although the absolute FWHM quantities for the low-density condition are not reliable due to fuel decomposition, we can still analyze the relative FWHM behavior along the length of the jet. Moreover, spreading angle trends discussed below do not change for any density if using a different spray width definition, *e.g.* 10% or 20%.) For reference, the model FWHM is also provided along with the spreading angle corresponding to the FWHM. Recall that the Gaussian-like profile used by the model has an equivalent FWHM spreading angle that is approximately 45% of the full ($Z = 0$) spreading angle used as an input.

The figure shows that the experimental FWHM growth is fairly linear at all ambient densities, but the slope of the line is greater than that of the model. In addition, the linear fit to the experimental data crosses zero at positive axial distances less than 10 mm from the injector. By contrast, the construct of the model (Fig. 1) forces a virtual origin at slightly negative axial distances. Obviously, the true spray origin cannot be a positive distance from the injector—by definition it is zero. Therefore, the spray spreading angle must change near the injector, starting with a small angle that transitions to a larger angle farther downstream. The experimental linear fit crosses zero at higher distances from the injector for lower ambient densities in Fig. 20, indicating that the spreading angle remains small for greater axial distance at low ambient density. Recent measurements of the spreading angle in the dense region of the spray near the nozzle corroborate this observation [34]. Others have shown that the "microscopic" spray angle near the nozzle is smaller than the "macroscopic" angle of the spray downstream [34,39,40]. The spreading angle tends to increase with increasing ambient density, but the transition to the larger spreading angle occurs at shorter distances from the injector as ambient density increases [34].

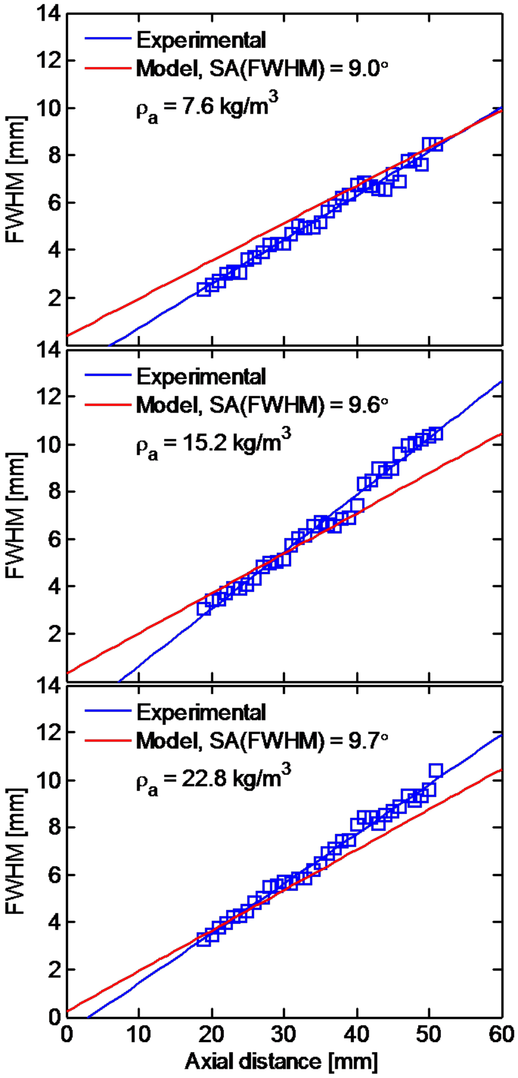

Figure 20: FWHM of vaporized spray as a function of ambient density. (top) 7.6 kg/m^3, (middle) 15.2 kg/m^3, (bottom) 22.8 kg/m^3. Injector conditions: 0.090-mm orifice, 150 MPa fuel pressure, n-dodecane, 363 K.

The linear fit of FWHM indicates that the spray angle is constant within the experimental data, suggesting that the transition to a larger spreading angle is finished at these axial distances. The slope of this fit is larger than that of the model, however. Still, at 15.2 kg/m^3 or 22.8 kg/m^3, the model jet width falls in the middle of the experimental data. As a result, the model tends to match the experimental radial distribution of mixture fraction for the examples shown in Figs. 16 or 19. However, areas where the model fails to follow the experimental data will occur when the experimental jet width is different than the model. In particular, the experimental jet width is larger than the model at 45 mm from the injector (see Fig. 16 for 15.2 kg/m^3). If the model spreading angle was increased, it could match the experimental jet width at 45 mm, and this would also reduce the centerline mixture fraction to better follow the decay in mixture fraction of the experimental data downstream of 45 mm. But since the model uses only a single spreading angle, the model would not capture the transition from narrow jet angle upstream to larger jet angle downstream. Therefore, the assumption of constant spreading angle may be a shortcoming of the current model.

While use of a single spreading angle in the model allowed adequate prediction of the jet penetration (and mixing), in fact, a spreading angle that transitions from a small angle to a larger angle with axial distance may explain subtle changes to the jet penetration rate that are not represented by the model. Penetration data from Fig. 11 show that jets initially penetrate at a faster rate than the model, but then change to a slower penetration rate than the model with increasing time ASI and increasing axial distance. The curves cross at about 1500 μs ASI at penetration distances of about 60 mm for the two lower ambient densities. This behavior can be explained by a spreading angle that transitions from low to high somewhere upstream, although the jet penetration does not respond immediately. Once again, the high-density condition at 22.8 kg/m^3 appears less-affected by changes in spreading angle as the measured and modeled penetration distance track together for an extended time. We would also like to point out that the effect of a spray/jet angle change on penetration distance is difficult to quantify, because the jet penetration responds to the integrated effect of these upstream changes of spray angle.

DISCUSSION

The quantitative measurements of mixing in evaporating diesel sprays, and the Musculus/Kattke model's success in predicting these measurements when using measured spray penetration data, is encouraging. Together they suggest the model has the potential for accurately representing mixing and other quantities that depend upon mixing, such as the liquid-phase penetration length. In addition, we can now extract new understanding about combustion process within these sprays. In particular, past combustion measurements using the same injector and at the same operating conditions can be interpreted in a new light. However, several assumptions of the model may not be justified at operating conditions that are significantly different than those presented in this study. Also, there are opportunities for improvement of the model. Examples of the new understanding and the various other issues listed above will be discussed below.

LIQUID LENGTH MEASUREMENTS AND PREDICTIONS

The model fuel jet of Musculus and Kattke has potential to be used to predict liquid-phase penetration and liquid length by exercising the assumption of mixing-limited vaporization in a manner similar to that done in Refs. [8,5]. These predictions may be possible without the need for constants that appears in the liquid length scaling law derived by Siebers [8], which were determined by fitting to experimental data.

Employing the mixing-limited assumptions, the liquid length can be assumed as the location on the spray centerline with a predicted mixture fraction that is equal to the mixture fraction for a saturated liquid-vapor equilibrium state arrived at when just enough hot ambient gas has been mixed with the fuel to fully vaporize the fuel. This mixture fraction is defined as Z_{sat} and depends solely upon fuel and ambient gas properties and their temperature and pressure [8]. However, to predict the centerline mixture fractions with the model, appropriate mixing data is needed from the nozzle to the liquid length. Since our quantitative mixing data is obtained only downstream of the liquid length, further information is needed to describe mixing and spreading angle changes in the near-field of the spray. The following example prediction of liquid length and comparison to the measured liquid length will illustrate some of the challenges and unknowns when employing the Musculus/Kattke model for liquid length.

The liquid length corresponding to the steady-state period of injection was measured by Mie-scatter imaging as described in the experimental section. For the conditions of Fig. 13, the measured liquid length is 11 mm [28] when processing the images with a signal intensity threshold of 3% of the maximum signal upstream in the spray, as used by Siebers [7]. Using the Musculus/Kattke model, the spreading angle measured downstream of the liquid in this paper (21.5°), and the assumptions discussed above, results in a smaller liquid length prediction than measured, however. This result is demonstrated in Fig. 21. Figure 21 shows the model centerline mixture fraction decay for spreading angles of 21.5° and 14.0°. The figure also shows that the Z_{sat} for these conditions is 0.34. Following the centerline mixture fraction decay down to Z_{sat} for a spreading angle of 21.5° gives a predicted liquid length of only 7.1 mm, which is much lower than the measured liquid length. To obtain the same liquid length as measured, a smaller spreading angle of

14° is required in the model.

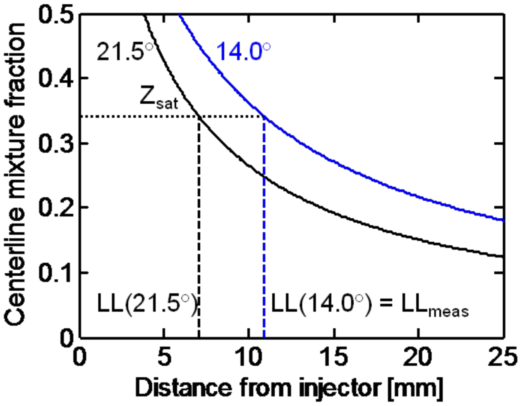

Figure 21: Predicted centerline mixture fraction showing the liquid length (LL) obtained with various spreading angles. Ambient conditions: 900 K, 22.8 kg/m^3, 6.0 MPa. Injector conditions: 0.090-mm orifice, n-dodecane, 363 K.

These results show that there is a difference in the spreading angle needed to predict liquid length and the spreading angle required to predict the mixture fraction distribution downstream in the vapor portion of the fuel jet. A larger spreading angle is needed for accurate prediction of downstream mixture fraction and jet penetration. A smaller spreading angle is needed for prediction of the liquid length, which is located closer to the nozzle. This trend was also observed for other fuels and ambient densities given in this paper. For example, the predicted liquid length for the conditions of Fig. 17 (n-heptane, 14.8 kg/m^3) using a 23° spreading angle is only 4 mm, whereas the measured liquid length is 9.5 mm.

Reasons for lack of agreement between the measured liquid length and the predicted using the far field spray region spreading angle are not entirely understood, but a potential contributing factor is likely a transition from a smaller to a larger spreading angle with distance downstream of the nozzle, as suggested by the results in Fig. 20. If the spreading angle is smaller near the nozzle, the liquid length would be more dependent upon this smaller spreading angle and the mixing it implies, as opposed to the larger angles measured downstream in this work. As mentioned above, this transition in spreading angle has recently been observed by *x*-ray measurement techniques in non-vaporizing sprays [34] and it is consistent with our results showing a positive x-axis intercept for the fit of FWHM data given in Fig. 20. It is also consistent with differences in the smaller spreading angles measured near the nozzle [34,39,40] and the larger spreading angles typical measured in this work and by many others much farther downstream of the injector orifice. A more detailed understanding of the transition in spreading angle is necessary to understand differences in spreading angle required for accurately representing the liquid-phase region, typically occurring closer to the injector, and that required for accurately representing vapor mixture development over the length of a spray, including the penetration of the spray.

The smaller spreading angles for prediction of measured liquid lengths are also consistent with the liquid length model of Siebers [8] and the spreading angles measured and used in conjunction with it. The spreading angles for all conditions in Ref. [8] were measured between the injector tip and a distance slightly longer than the measured liquid length, essentially providing an average spreading angle over just the liquid length region of the spray, not the downstream region of the fuel jet as in the present paper. However, also note that the spreading angle measurement technique and method of determination from images in the earlier liquid length research of Siebers are different from the present work. As a result, interchanging spreading angle measurements between Siebers [8] and the present work is not appropriate, as is the case for most spreading angle data in the literature. More will be stated on this point in the next section.

LOCAL MIXTURE EQUIVALENCE RATIO AND SOOT FORMATION

Past research in our laboratory has addressed the subject of soot formation in diesel sprays [38,41,42], and its connection to flame lift-off length [43,44]. For this research, the DDC injector described earlier was fitted with single axial-hole nozzles of various size, including the 0.100-mm diameter orifice of this study. To aid interpretation of the measurements, the model of Naber and Siebers was used to estimate the amount of ambient gas entrained into a fuel jet upstream of the lift-off length. Since this model is based on uniform radial distributions for mixing and velocity, the oxygen entrained into the spray relative to the fuel injected was expressed in terms of the cross-sectionally averaged equivalence ratio, $\overline{\phi}$, implied by their model and defined in Eqs. (4)-(5).

$$\overline{\phi} = \frac{2 \cdot (A/F)_{st}}{\sqrt{1 + 16 \cdot \left(\frac{x}{x^{+}}\right)^{2}} - 1} \qquad (4)$$

In Eq. (4), $(A/F)_{st}$ is the ambient-to-fuel stoichiometric ratio by mass, and x^{+} is a characteristic length scale for the fuel jet, defined as:

$$x^{+} = \sqrt{\frac{\rho_f}{\rho_a}} \frac{\sqrt{C_a} \cdot d}{a \cdot \tan(\theta/2)} . \qquad (5)$$

The constant *a* is needed to relate the measured spreading angle to the model angle, thereby accounting for "real" velocity and mass radial distribution effects compared to the uniform profile assumed by the model. The constant was adjusted to give the best fit between non-vaporizing spray penetration data and predictions from the Naber/Siebers model [3]. Originally, *a* was assigned a value of 0.66 [3], but this was later changed to a value of 0.75 based on more accurate measurements of the orifice flow coefficients [44]. Equations (4) and (5) show that estimates for $\overline{\phi}$ depend upon model inputs for spreading angle, similar to the Musculus/Kattke model used in the current study. However, the Musculus/Kattke model has the option for a realistic velocity and mass radial distributions and does not require the model constant *a*.

Spreading angles used for prediction of ambient entrainment into the spray in earlier studies were measured by schlieren imaging [3,8]. The spreading angles used for later studies on lift-off length and soot formation were actually first measured for studies of liquid length in evaporating sprays [7,8]. As the focus for the evaporating spray studies was understanding liquid-phase penetration, analysis of time-averaged schlieren images was limited to distances only slightly downstream of the liquid length, as previously mentioned. Also, no vapor penetration data were taken. In addition, spreading angles were defined using a threshold intensity midway between the intensity of the average background and the spray centerline, which is a different method than that used in this study. For the 0.100-mm nozzle at the same ambient density and temperature used in this study (14.8 kg/m^3, 1000 K), the measured full spreading angle (θ) was 13.0° in Ref. [8]. This is obviously much smaller than the 24.0° angle (see Fig. 7 and Table 5) measured further downstream after the liquid length using the time-resolved, high-sensitivity schlieren setup in this study, but it agrees with the angles necessary for prediction of the liquid length (see Fig. 21). A contributing factor for the larger measured spreading angle in this paper is that more of the far-field of the jet is considered. Vapor boundaries up to an axial distance of 50 mm were used to determine the spreading angle in this study, which is well beyond the 9.6 mm liquid length for an n-heptane spray at this condition. For prediction of mixing downstream in the jet, this larger angle is more appropriate, and more consistent with spreading angles needed to match the vapor penetration. Figure 17 shows that a spreading angle of 23° gave model predictions of mixture fraction that are in close agreement with results obtained by Rayleigh scattering. This angle also results in accurate predictions of the measured vapor penetration (Fig. 10).

With a direct measurement of mixing, we now have the opportunity to compare past predictions of $\overline{\phi}$ with Eqs. (4)-(5) to the actual measured equivalence ratio values from the present paper. A significance of this new comparison is that past research showed that fuel jets became non-sooting when $\overline{\phi}$ decreased below a value of approximately two [38,43,44]. However, a fuel mixture fraction profile like that assumed in Eq. (1) suggests that the jet centerline ϕ would be much higher than two, 3.8 times higher for $\alpha = 1.5$ and use of the full cross-sectional area of the jet (to $\phi(R) = 0$) to compute $\overline{\phi}$ [4]. The result of a local centerline of 7.6 (twice 3.8) is clearly inconsistent with wide ranging experimental data showing soot disappearing at a ϕ of about two [45]. Ultimately, the calculation of $\overline{\phi}$ is highly dependent upon the radial limit of integration, or effectively, the local mixture for a particular definition of spreading angle. Since past research had a particular method for determination of spreading angle, as described above, the mixing measurements will serve to calibrate the actual local ϕ, perhaps that at the jet centerline, compared to the calculated $\overline{\phi}$. As more narrow spreading angles were used to compute $\overline{\phi}$, and the constant *a* further narrows the angle for use in Eqs. (4)-(5), our expectation is that the centerline ϕ will be less than a factor of 3.8 greater than $\overline{\phi}$.

A simple way to display the actual equivalence ratios in the jet, at least in the far field, is to use the Musculus/Kattke model predictions at a spreading angle of 23° and the experimental conditions of Fig. 17, since these mixing predictions matched the experimental data at these conditions (0.100-mm nozzle, n-heptane, 14.8 kg/m^3). A contour plot of equivalence ratios is shown at the top of Fig. 22 for an ambient gas oxygen mole fraction of 21%. A detailed set of lift-off length and soot mass distribution within the jet was previously obtained at this same ambient density, oxygen concentration, and fuel, for various ambient temperatures [41,42] and are shown at the bottom of Fig. 22. The soot mass measurements were made at a fixed axial distance of 50 mm from the injector, which is the peak soot location [41], providing an indication of the sooting propensity of the entire jet. They are plotted against lift-off length for each dataset to show how changes in lift-off length affect soot formation. The figure shows that for an ambient temperature decrease, the lift-off length increases and the corresponding soot mass decreases and becomes zero at a lift-off length of 30 mm. The soot mass is shown on a highly resolved *y*-axis scale (left) to illustrate the sudden transition from sooting to non-sooting combustion with increasing lift-off length.

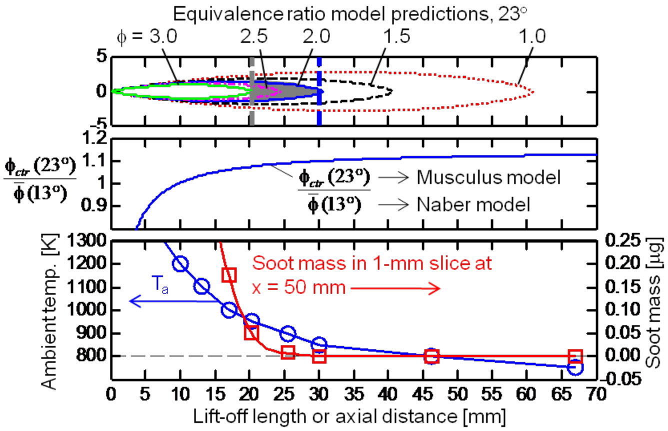

Figure 22: (top) Contour plot of equivalence ratio based on model predictions with a spreading angle of 23° and tuned by measurements. (middle) comparison of centerline ϕ to past estimates of $\bar{\phi}$. (bottom) Ambient temperature and soot mass for a given lift-off length. Experimental conditions the same as Fig. 17, except ambient oxygen concentration is 21% and ambient temperature is varied.

Two lift-off lengths corresponding to two different ambient temperatures in this sooting/non-sooting transition region are shown as vertical dashed lines on the top equivalence-ratio contour plot (at 21 mm for 950 K and 30 mm for 850 K). When the lift-off length is 30 mm, all of the mixtures downstream of the lift-off length, at any axial or radial position, have equivalence ratio values less than two. The most fuel-rich mixture at 30 mm is ϕ = 2 at the centerline. Consequently, when combustion (*i.e.*, the lift-off) begins at 30 mm there has already been enough mixing to produce mixtures that are too fuel-lean for soot formation, consistent with the soot measurements shown. Note that an axial distance of 30 mm is within the limits of our experimental mixing measurement (Fig. 17). Because we see excellent agreement between the jet model and experimental mixture fraction distribution at this location, confidence is high that the centerline mean equivalence ratio at this axial location is, in fact, less than two. By contrast, when the lift-off length is 20 mm, mixtures downstream of the lift-off length have equivalence ratio values as high as three. The region of the fuel jet that is likely to burn with fuel-rich, soot-forming mixtures (ϕ> 2) for a lift-off length of 20 mm is shown as a gray shaded region. The gray region indicates that there is substantial opportunity for soot formation, and so it is no surprise that soot is measured downstream at 50 mm, before the soot can be fully oxidized. As lift-off length decreases further, the amount of upstream, fuel-rich mixtures that would form soot continues to increase. As a result, the measured soot mass within the jet continues to increase.

Past analysis of Rayleigh scattering measurements taken at these same experimental conditions, but in the transient head of the jet at the time of ignition, reached the same conclusion [23]. As temperature increases, the mixture that ignites during the premixed burn becomes progressively more fuel-rich, thereby forming more soot. At an ambient temperature of 850 K, the premixed burn mixture equivalence ratio distribution is mainly less than two and soot formation is avoided [23]. In summary, the direct measurements of mixing are consistent with an understanding of soot formation in partially-premixed fuel jets when considering local equivalence ratio. The relationship appears valid for both steady and transient, igniting jets.

The new mixing data demonstrates that the measured equivalence ratio at the centerline of the jet is actually very close to past estimates for $\bar{\phi}$. Hence, the transition to non-sooting combustion occurs when either the centerline ϕ, or the (past) estimated $\bar{\phi}$, is lower than a value of approximately two. The ratio of the centerline ϕ to past estimates for $\bar{\phi}$ is shown at the middle of Fig. 22. After a short transition period very near the nozzle (when $\alpha > 1.5$ [4]), the centerline ϕ predicted by the Musculus/Kattke model using a 23° spreading angle is approximately 10-15% higher than $\overline{\phi}$ calculated by the Naber/Siebers model using the measured angle of 13°. The difference in spreading angle measurement compared with the present experiment and the calibration of the constant in Eq. (5) with penetration data and liquid length data (both occurring along the centerline of the fuel jet) most likely explain the closeness between centerline ϕ and $\overline{\phi}$ defined by Eqs. (4)-(5). This result once again elucidates the point that spreading angle is not a robust measurement, and should not be used external to the data they were developed for unless there is a clear understanding of the relationship between the spreading angle and the radial fuel concentration profiles in the observed fuel spray. Clearly, a true cross-sectional average would not have nearly the same value as the centerline. As a result, the past approximation for $\overline{\phi}$ should no longer be thought of as a cross-sectional average. We made similar arguments when generating a model for the radial distribution of mixture fraction to understand soot formation near the lift-off length in Ref. [46]. Mainly by deduction using measured soot trends, we chose the centerline ϕ to be 30% higher than our past estimate for $\overline{\phi}$, which in retrospect appears to have been a fair approximation.

While results are shown here for specific operating conditions at which there was mixing, soot, and lift-off length data, the finding of a relationship between past estimates for $\overline{\phi}$ and the measured centerline ϕ, and that the two values are similar in magnitude is significant. For example, this relationship allows a better understanding of the transition to non-sooting combustion at other conditions where no mixing data is available. As mentioned above, past research has shown that fuel jets become non-sooting when $\overline{\phi} < 2$ (past estimates for $\overline{\phi}$). But the past dataset is very extensive, including injector parameters such as orifice diameter and injection pressure [43], and ambient gas parameters such as temperature, density, and oxygen concentration [42-44] where no mixing data is available. The implication is that $\overline{\phi}$ is close to the centerline ϕ for these conditions as well, at least for conditions where $\overline{\phi} \approx 2$. A cautionary note should also be made though. The close relationship of $\overline{\phi}$ and the centerline ϕ noted is not a given for regions of the fuel jet where the profile given by Eq. (1) isn't approximately valid, such as potentially in the upstream near field region of the fuel jet which Figs. 20-21 suggested has smaller spreading angles. In such regions, the net result could be a different relationship between past estimates for $\overline{\phi}$ and the actual centerline ϕ.

SUMMARY/CONCLUSIONS

In the current work, quantitative measurements of the fuel mixture fraction in evaporating diesel sprays are used to assess the accuracy of the Musculus/Kattke model with radial and axial prediction of fuel-ambient mixture. Quantitative mixture fraction measurements by Rayleigh-scatter imaging are coupled to measurements of spray global quantities by high-speed schlieren imaging such as vapor-phase penetration and spreading angle in a high-temperature, high-pressure vessel. The liquid-phase penetration length and nozzle flow coefficients are also measured. The experimental conditions span a range of ambient densities, fuels, nozzle sizes, and nozzle shapes to address the robustness of the models at various conditions. Mixing measurements are obtained during the steady-state, fully developed period of fuel injection. The following conclusions are reached by this study:

- Schlieren measurements of vapor jet spreading angle exhibit a strong sensitivity to optical setup and image processing routines. Interpreted spreading angles change by several degrees, creating uncertainty as to the appropriate spray model input. However, schlieren measurements of jet penetration are not sensitive to optical setup.
- Spreading angles based on measurement of a high-sensitivity schlieren optical setup are needed as inputs to the Musculus/Kattke model to obtain a match between modeled and measured fuel spray penetration. The model input angle is the full spreading angle where the radial distribution of fuel mixture fraction goes to zero, suggesting that a schlieren optical setup with high-sensitivity measures low concentration of fuel vapor. Quantitative Rayleigh scattering measurements confirm these observations.
- Results over a wide range of conditions suggest that the ambient entrainment into the model should be based on measured spray penetration, not spreading angle. It is much easier to use measured spray penetration, coupled with model predictions for spray penetration, to determine the spreading angle for the spray, rather than using less accurate (or repeatable) schlieren measurements of spray angle.
- Using the same spreading angle that matched jet penetration, the model predictions also produce local mixture fractions that are generally within the Rayleigh scattering experimental uncertainty. Accurate model predictions of mixture fraction are achieved for a range of ambient densities, fuel injector nozzle shapes, injection pressures, and types of fuels. These results show that the radial distribution used in the Musculus/Kattke model, which resembles a Gaussian error function, is an appropriate representation of mixture fraction in a fully developed, vaporized diesel spray.
- The experimental (and model) mixture fraction for vaporized diesel sprays follows a self-similar distribution. The centerline mixture fraction decays inversely proportional to axial distance, and collapses when normalized by the jet outer radius. While

these are well-known results for gas jets, this study is the first to convincingly demonstrate that vaporized diesel sprays are also self-similar.

- Extrapolation of the mixing measurements suggests that a diesel fuel spray has a smaller spreading angle in the near-field and transitions to a larger angle in the far-field. The transition to the larger spreading angle occurs at shorter distances from the injector as ambient density increases. Since the current version of the Musculus/Kattke model assumes a constant spreading angle, there is an opportunity to improve the model with a more detailed understanding of the transition in spreading angle.
- Consistent with this observation, use of far-field spreading angles that successfully match mixture fraction and jet penetration, causes underprediction of experimentally measured liquid lengths that extend through the near field, typically into the transition between the near- and the far- field.
- The new mixing data provides an opportunity to evaluate past measurements of ambient entrainment based on the one-dimensional Naber/Siebers model that were used for interpretation of combustion (lift-off length and soot) measurements at the same operating conditions. Results show that past estimates for the cross-sectionally averaged equivalence ratio using the Naber/Siebers model are only 10-15% lower than the measured centerline equivalence ratio, at least in the far field of jet where the centerline equivalence ratio is near a value of two. Quantification of the actual centerline equivalence ratio explains the transition from sooting to non-sooting combustion observed previously.

The quantitative measurements of mixing in evaporating diesel sprays, and the success in using the Musculus/Kattke model for prediction of these measurements when using measured jet penetration data, is encouraging. The results suggest that the measured jet penetration in the vaporized portion of the fuel spray can be used as the primary estimate for ambient entrainment in the far field of the spray. When coupled to a simplified mixing model, accurate estimates of mixing are available for further interpretation of vaporization and combustion, including transients during or after the end of injection. However, further insight is needed to explain spray mixing in liquid regions of the spray that were inaccessible to the quantitative mixing measurement by Rayleigh scattering. Existence of smaller spreading angles in the near-field of the spray are believed to be the source of the inconsistency for liquid length predictions when using far-field measured spreading angles. The need for improved understanding spray near- and far-field mixing characteristics is clearly indicated.

REFERENCES

1. Peters, N. and Weber, J., "The Effects of Spray Formation and Evaporation on Mixing, Auto-ignition and Combustion in Diesel Engines," THIESEL 2006, Valencia Spain.
2. Baert, R., Frijters, P., Somers, B., and Luijten, C., "Design and Operation of a High Pressure, High Temperature Cell for HD Diesel Spray Diagnostics: Guidelines and Results," SAE Paper 2009-01-0649, 2009.
3. Naber, J.D. and Siebers, D.L., Paper 960034:"Effects of Gas Density and Vaporization on Penetration and Dispersion of Diesel Sprays," SAE Trans. 105(3):82-111, 1996.
4. Musculus, M.P.B. and Kattke, K., Paper 2009-01-1355:"Entrainment Waves in Diesel Jets," *SAE Int. J. Engines* 2:1170-1193, 2009.
5. Kook, S., Pickett, L.M., Musculus, M.P.B., and Gehmlich, R. K., Paper 2009-01-1356:"Influence of Diesel Injection Parameters on End-of-Injection Liquid Length Recession," *SAE Int. J. Engines* 2:1194-1210, 2009.
6. Abramovich, G. N., "Chapter 5: Jet of an Incompressible Fluid in a Coflowing External Stream," The Theory of Turbulent Jets, The MIT Press, Cambridge, MA, USA, 1963.
7. Siebers, D.L., Paper 980809:"Liquid-phase fuel penetration in diesel sprays," *SAE Trans*. 107:1205-1227, 1998.
8. Siebers, D.L. Paper 1999-01-0528:"Scaling Liquid-Phase Fuel Penetration in Diesel Sprays Based on Mixing-Limited Vaporization." *SAE Trans*. 108(3):703-728, 1999.
9. Desantes, J.M., Payri, R., Salvador, F.J., and Gimeno, J., "Measurements of Spray Momentum for the Study of Cavitation in Diesel Injection Nozzles," SAE Paper 2003-01-0703, 2003.
10. Payri, R., Salvador, F.J., Gimeno, J., and Zapata, L.D., "Diesel Nozzle Geometry Influence on Spray Liquid-Phase Fuel Penetration in Evaporative Conditions," *Fuel* 87:1165-1176, 2008.
11. Abdelghaffar, W.A., Karimi, K., and Heikal, M.R., "Fuel Spray Penetration in High-Pressure Diesel Engines," SAE Paper 2007-01-0066, 2007.
12. Karimi, K., Sazhina, E.M., Abdelghaffar, W.A., Crua, C., Cowell, T., Heikal, M.R., and Gold, M.R., "Developments in Diesel Spray Characterisation and Modelling," Thermo- and Fluid-Dynamic Processes in Diesel Engines: THIESEL, Valencia, Spain, 2006.
13. Egermann, J., Göttler, A., and Leipertz, A., "Application of Spontaneous Raman Scattering for Studying the Diesel Mixture Formation Process Under Near-Wall Conditions," SAE Paper 2001-01-3496, 2001.

14. Aronsson, U., Chartier, C., Andersson, O., Egnell, R., Sjoholm, J., Richter, M., and Alden, M., "Analysis of the Correlation Between Engine-Out Particulates and Local Equivalence Ratio in the Lift-Off Region of a Heavy Duty Diesel Engine Using Raman Spectroscopy," SAE Paper 2009-01-1357, 2009.
15. Kim, T. and Ghandhi, J.B., "Characterization of evaporating diesel sprays using exciplex laser-induced fluorescence measurements," *Atom. Sprays* 13:535-559, 2003.
16. Bruneaux, G., "Mixing Process in High Pressure Diesel Jets by Normalized Laser Induced Exciplex Fluorescence Part I: Free Jet," SAE Paper 2005-01-2100, 2005.
17. Payri, F., Pastor, J.V., Pastor, J.M., and Julia, J.E., "Diesel Spray Analysis by Means of Planar Laser-Induced Exciplex Fluorescence," *Int. J. Engine Research* 7:77-89, 2006.
18. Kosaba, H., Kamimoto, T., “Quantitative Measurement of Fuel Vapor Concentration in an Unsteady Evaporating Spray via a 2-D Mie-Scattering Imaging Technique,” SAE Paper 932653, 1993.
19. Bruneaux, G., “Liquid and Vapor Spray Structure in High-pressure Common Rail Diesel Injection,” *Atom. Sprays*, 11:533, 2001.
20. Espey, C., Dec, J.E., Litzinger, T.A., and Santavicca, D.A., "Planar Laser Rayleigh Scattering for Quantitative Vapor-Fuel Imaging in a Diesel Jet," *Combust. Flame* 109:65-86, 1997.
21. Schulz, C., Gronki, J., and Andersson, S., "Multi-Species Laser-Based Imaging Measurements in a Diesel Spray," SAE Paper 2004-01-1917, 2004.
22. Adam, A., Leick, P., Bittlinger, G., and Schulz, C., "Visualization of the Evaporation of a Diesel Spray using Combined Mie and Rayleigh Scattering Techniques," *Exp. Fluids* 47:439-449, 2009.
23. Idicheria, C.A. and Pickett, L.M., "Quantitative Mixing Measurements in a Vaporizing Diesel Spray by Rayleigh Imaging," SAE Paper 2007-01-0647, 2007.
24. Engine Combustion Network data archive. <http://www.sandia.gov/ECN/>.
25. Abraham, J. and Pickett, L.M., "Computed and Measured Fuel Vapor Distribution in a Diesel Spray," *Atom. Sprays* 20:241-250, 2010.
26. Pickett, L.M., Kook, S., and Williams, T.C., Paper 2009-01-0658:"Visualization of Diesel Spray Penetration, Cool-Flame, Ignition, High-Temperature Combustion, and Soot Formation Using High-Speed Imaging," *SAE Int. J. Engines* 2:439-459, 2009.
27. Settles, G.S., *Schlieren and Shadowgraph Techniques*, Springer-Verlag, 2001.
28. Pickett, L.M., Genzale, C.L., Bruneaux, G., Malbec, L.-M., Hermant, L., Christiansen, C.A., and Schramm, J., "Comparison of Diesel Spray Combustion in Different High-Temperature, High-Pressure Facilities," SAE Paper 2010-01-2106, 2010.
29. d’Errico, J. Inpaint_nans routine. Matlab file exchange, <http://www.mathworks.com/matlabcentral/fileexchange/?term=tag%3A%22inpaint%22>, 2006.
30. Dibble, R.W., Hollenbach, R.E., “Laser Rayleigh Thermometry in Turbulent Flames”, *Proc. Combust. Inst.*, 18:1489, 1980.
31. Pickett, L.M., Caton, J.A., Musculus, M.P.B., and Lutz, A.E., "Evaluation of the Equivalence Ratio-Temperature Region of Diesel Soot Precursor Formation using a Two-Stage Lagrangian Model," *Int. J. Engine Res.*7:349-370, 2006.
32. Moffat, R.J., "Describing the Uncertainties in Experimental Results," *Exp. Therm. Fluid Science* 1:3-17, 1988.
33. Blessing, M., König, G., Krüger, C., Michels, U., and Schwarz, V., "Analysis of Flow and Cavitation Phenomena in Diesel Injection Nozzles and its Effects on Spray and Mixture Formation," SAE Paper 2003-01-1358, 2003.
34. Kastengren, A.L., Powell, C.F., Wang, Y.J., Im, K.S., and Wang, J., "X-Ray Radiography Measurements of Diesel Spray Structure at Engine-Like Ambient Density," *Atom. Sprays* 19:1031-1044, 2009.
35. Arrègle, J., Pastor, J.V., and Ruiz, S., "The Influence of Injection Parameters on Diesel Spray Characteristics," SAE Paper 1999-01-0200, 1999.
36. Hiroyasu, H. and Arai, M., "Structures of Fuel Sprays in Diesel Engines," *SAE Trans.* 99:1050-1061, 1990.
37. Payri, F., Desantes, J.M., and Arrègle, J., "Characterization of DI diesel sprays in High Density Conditions," SAE Paper 960774, 1996.
38. Pickett, L.M. and Siebers, D.L., "Soot in Diesel Fuel Jets: Effects of Ambient Temperature, Ambient Density, and Injection Pressure," *Combust. Flame* 138:114-135, 2004.
39. Heimgärtner, C. and Leipertz, A., "Investigation of the Primary Spray Breakup Close to the Nozzle of a Common – Rail High Pressure Diesel Injection System," SAE Paper 2000-01-1799, 2000.
40. Reitz, R.D. and Bracco, F.B., “On the Dependence of Spray Angle and Other Spray Parameters on Nozzle Design and Operating Conditions,” SAE Paper 790494, 1979.
41. Pickett, L.M. and Idicheria, C.A., "Effects of Ambient Temperature and Density on Soot Formation under High EGR Conditions," Thermo- and Fluid-Dynamic Processes in Diesel Engines: THIESEL, Valencia, Spain, 2006.
42. Idicheria, C.A. and Pickett, L.M., Paper 2005-01-3834:"Soot Formation in Diesel Combustion under High-EGR Conditions," *SAE Trans.* 114:1559-1574, 2005.
43. Siebers, D.L. and Higgins, B.S., Paper 2001-01-0530:"Flame Lift-Off on Direct-Injection Diesel Sprays under Quiescent Conditions," *SAE Trans.* 110:400-421, 2001.

44. Siebers, D.L., Higgins, B.S., and Pickett, L.M., Paper 2002-01-0890:"Flame Lift-Off on Direct-Injection Diesel Fuel Jets: Oxygen Concentration Effects," *SAE Trans.* 111:1490-1509, 2002.
45. Heywood, J., *Internal Combustion Engines*, McGraw-Hill, New York, 1988.
46. Pickett, L.M. and Siebers, D.L., "Soot Formation in Diesel Fuel Jets Near the Lift-Off Length," *Int. J. Engine Res.* 7:103-130, 2006.
47.

CONTACT INFORMATION

Lyle M. Pickett: LMPicke@sandia.gov

ACKNOWLEDGMENTS

Support for this research was provided by the U.S. Department of Energy, Office of Vehicle Technologies. The research was performed at the Combustion Research Facility, Livermore, California. Sandia is a multiprogram laboratory operated by Sandia Corporation, a Lockheed Martin Company, for the United States Department of Energy's National Nuclear Security Administration under contract DE-AC04-94AL85000.

APPENDIX A: STEADY-JET MIXING AND PENETRATION

The model jet depicted in Fig. 1 with multiple control volumes is for transient jets with arbitrary injection rates. This solution is more general, but it requires numerical analysis for the mass and momentum exchange between control volumes [4]. However, when the rate of injection is steady, as is the case for the injectors used in this study, the fuel distribution representing a fully developed steady-state jet is available from an analytical solution. Also, as will be shown below, the steady-jet penetration solution is obtained with fairly simple, one-step numerical integration. Naber and Siebers [3] found similar analytical solutions for mixing and penetration. Here, we show these steady-state expressions for the Musculus and Kattke model [4], which incorporates a radial mixture profile and a transition region near the injector. These steady-state mixing and penetration solutions are used throughout this paper for comparison to experimental results.

The steady-state solution for the velocity and fuel distribution is given in Appendix A of Ref. [4]. The fuel liquid volume fraction χ_f and velocity u are related with equations (A4) and (A6) from Ref. [4]:

$$\overline{\overline{\chi}}_f = \frac{\dot{m}_{f,0}}{\rho_f \beta \overline{\overline{u}} A} \qquad \text{(A1)}$$

$$\overline{\overline{u}} = \dot{m}_{f,0} \frac{-\left(1 - \frac{\rho_a}{\rho_f}\right) + \sqrt{\left(1 - \frac{\rho_a}{\rho_f}\right)^2 + 4\beta \frac{\rho_a}{\rho_f} \frac{A}{A_0}}}{2\beta \rho_a A} \qquad \text{(A2)}$$

where the double overbars signify averages over the jet cross-section, subscript 0 indicates conditions at the nozzle exit, $\dot{m}_f$ is the fuel mass flow rate, and A is the control volume area. The term β is given by Eq. (5c) of Ref. [4].

$$\beta = \frac{6(\alpha + 1)(\alpha + 2)}{(3\alpha + 2)(2\alpha + 1)} \qquad \text{(A3)}$$

It depends only on the shape of the fuel mass distribution according to Eq. (1), ranging from $\beta = 1$ for a uniform profile near the nozzle (with $\alpha = \infty$) to approximately $\beta = 2$ for a fully developed jet (with = 1.5). The transition of α (and β) with respect to axial distance is described in Appendix B of Ref. [4], but the transition to a fully developed jet typically occurs within a few millimeters of the injector.

Describing the effective nozzle flow area A_0 relative to the physical diameter d_0 using the area-contraction coefficient C_a,

$$A_0 = \frac{C_a \pi d_0^2}{4} \qquad \text{(A4)}$$

the downstream jet area based on the spreading angle,

$$A = \pi R^2 = \pi(\tan(\theta/2)x')^2 \qquad \text{(A5)}$$

and combining (A1) and (A2) gives

$$\bar{\bar{\chi}}_f = \frac{2\frac{\rho_a}{\rho_f}}{-\left(1-\frac{\rho_a}{\rho_f}\right)+\sqrt{\left(1-\frac{\rho_a}{\rho_f}\right)^2+\frac{16\,\beta}{C_a}\frac{\rho_a}{\rho_f}\frac{(\tan(\theta/2)x')^2}{d_0^2}}} \quad , \qquad \text{(A6)}$$

which describes the steady-state mixing solution with respect to axial distance. Note that the form of this cross-sectionally averaged expression mimics Eq. (C32), given in non-dimensional coordinates by Naber and Siebers [3]. The liquid volume fraction also exhibits an approximate $1/x$ decay in Eq. (A6).

From Eq. (4a) of Ref. [4], the centerline and cross-sectionally averaged terms are related as

$$\bar{\chi}_{f,c} = \frac{(\alpha+1)(\alpha+2)}{\alpha^2}\bar{\bar{\chi}}_f \quad . \qquad \text{(A7)}$$

Through Eqs. (1) - (3), the fuel liquid volume fraction can then be used to provide a local mixture fraction prediction at any axial and radial location of the jet.

The derivation of the jet penetration time for constant rate of injection was already performed in Appendix A of Ref. [4]. Starting with Eq. (A9) from Ref. [4] and performing substitutions for (A4) and (A5) above, the time of penetration relation to axial distance is

$$t = \frac{\left(1-\frac{\rho_a}{\rho_f}\right)}{2\beta\bar{\bar{u}}_0}\int\left(1+\sqrt{1+\left(\sqrt{\frac{16\pi\beta}{C_a d_0^2}\frac{\rho_a}{\rho_f}}\,\frac{\tan(\theta/2)x'}{\left(1-\frac{\rho_a}{\rho_f}\right)}\right)^2}\right)dx\,. \qquad \text{(A8)}$$

APPENDIX B: RAYLEIGH SCATTERING ISSUES

In this section we discuss several of the improvements made to the Rayleigh-scatter imaging diagnostic since the time of [23]. Operation at high ambient temperature in order to minimize the penetration of liquid droplets also caused new uncertainties about fuel decomposition that are addressed here.

THEORY

Figure B1 shows a composite of a Mie scattering image (left) and a Rayleigh scattering image (upper right). The Mie scatter and Rayleigh scatter images are shown as a composite, but they were actually obtained at different instances and with different experimental setups. The Mie scattering imaging setup was discussed above. As the spray entrains and mixes with the hot ambient, all of the liquid fuel is eventually vaporized at a location defined as the maximum liquid penetration length, or liquid length. For the conditions of Fig. B1, the liquid length is 9.5 mm. Knowing this maximum extent of liquid penetration, a laser sheet was then moved downstream of the liquid droplet region to provide Rayleigh scattering from fuel vapor and ambient gases without interference from liquid droplets.

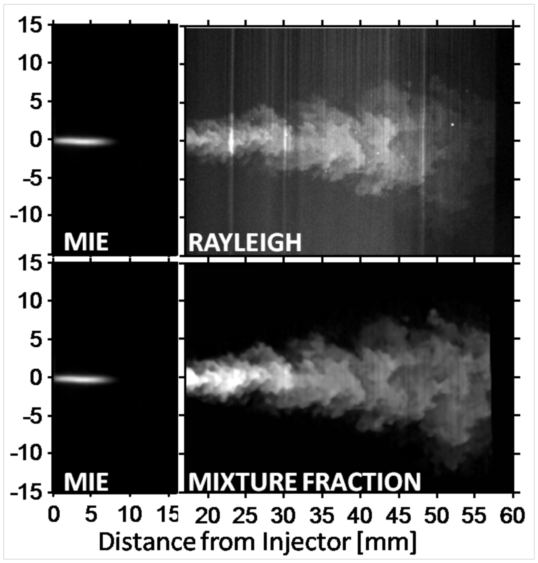

Figure B1: Composite image of Mie scattering (left) and Rayleigh scattering (right). Ambient conditions: 1000 K, 14.8 kg/m^3, 4.2 MPa, 0% O_2. Injector conditions: 0.100-mm orifice, 154 MPa, n-heptane. 6 ms ASI.

A significant advantage of implementing the Rayleigh technique in the constant-volume combustion vessel is the ability to simultaneously measure the signal from the ambient and the jet, as shown in the top-right image in Fig. B1. The measurement of the unmixed ambient just outside of the jet serves as a built-in calibration to correct for beam steering and laser intensity distribution. These laser intensity variations are clearly apparent in Fig. B1. Not only is the incoming laser intensity non-uniform, but as the laser beam propagates through the vaporized fuel jet from bottom to top there is additional beam steering caused by temperature variation within the jet. However, the simultaneous measurement of a Rayleigh signal from uniform ambient gases, as well as vaporized jet, provides a means for correction of beam steering and laser intensity distribution variation on a shot-by-shot basis. To indicate the success of these corrections, we show the fuel-ambient mixture fraction obtained by analysis of the Rayleigh scattering at the bottom left of Fig. B1. The analysis is described briefly below.

As the ambient gases surrounding the jet consist of known constituents with known Rayleigh cross-sections (see Table B1) and known temperature and pressure, the Rayleigh signal from the unmixed ambient can be written as:

$$I_{R,a} = \eta I_l N_{a,o} \sigma_a , \qquad \text{(B1)}$$

where η is the signal collection efficiency, I_l is the laser intensity, $N_{a,o}$ is the number density of the ambient (outside the jet) and σ_a is the mole-fraction-weighted Rayleigh cross-section of the ambient (5.61 x 10-27 cm^2). In the vapor region of the jet, the Rayleigh signal is generated by the same laser beam and from a binary mixture of the ambient and fuel vapor ($N_{mix}=N_a+N_f$) (Note that N_a is not the same as $N_{a,o}$). In the jet region the scattered intensity is:

$$I_{R,j} = \eta I_l N_{mix} \left\lfloor X_f \sigma_f + X_a \sigma_a \right\rfloor \qquad \text{(B2)}$$

As $X_a+X_f=1$ and according to the ideal gas law $N_{mix}/N_{a,o}=T_a/T_{mix}$ (T_a is the ambient temperature outside the jet and T_{mix} is the temperature of the fuel-ambient mixture), dividing Eq. (B2) by Eq. (B1) yields:

$$\frac{I_{R,j}}{I_{R,a}} = \left(\frac{\sigma_f/\sigma_a + N_a/N_f}{1 + N_a/N_f} \right) \frac{T_a}{T_{mix}} . \qquad \text{(B3)}$$

By assuming adiabatic mixing between the ambient and liquid fuel at known thermodynamic conditions, application of conservation of energy shows that $T_{mix} = f(N_a/N_f)$ [20]. Therefore, one may solve for N_a/N_f by utilizing this functional dependence for T_{mix} in Eq. (B3) and measuring the Rayleigh signal from the jet and ambient. Converting between fuel-ambient number ratio N_a/N_f and mass ratio *F*/*A* using molecular weight, one arrives at the fuel mass fraction or mixture fraction Z with Eq. (1). The *F*/*A* can be converted to an effective equivalence ratio ϕ using the stoichiometric *F*/*A* ratio for the fuel and ambient.

Table B1. Ambient gas and fuel Rayleigh cross-sections.

	N_2	CO_2	H_2O	nC7	nC12
σ_i x 10^{-27} [cm^2]	5.23	12.02	3.66	309.80	851.90

INTERFERENCES FROM WINDOWS AND PARTICLES

One of the challenges of the Rayleigh-scatter imaging technique is that the signal and incident light are of the same wavelength. Avoiding interference from other sources of elastic scatter (other than the fuel and ambient) is critical to the success of the measurement. Examples of potential sources of elastic scattering include particles or contaminants in the fuel and ambient, fuel droplets, and reflectance and scattering from optical windows and laser-sheet delivery optics. Extreme care must be taken to prevent interference from these noise sources. Steps to remove unwanted background laser flare were discussed in detail in [23].

Since the time of [23], we have implemented several improvements to the optical setup that have improved signal and reduced laser flare even more. These improvements benefit experiments for the newer, 0.090-mm orifice (see table 4). Signal is improved by using a higher quantum efficiency sensor and faster camera lens (f/1.4). In addition, special laser transmitting and receiving windows are utilized, consisting of 7×58 mm fused-silica “slits” mounted in a circular metal geometry fit to the normal window port as shown in Fig. B2. The metal is coated with absorptive carbon black inside the vessel to reduce reflection. Beam blocks with a “slit” geometry are also attached outside the windows where the laser sheet enters and exits to reduce reflections from transmitting optics. The new fused-silica slits have less reflection and scatter because of the lower refractive index of fused silica (1.46) compared to sapphire (1.77) at 532 nm. The coating above the transparent slit is also more effective at reducing laser scatter by absorption compared to specular-reflective window surfaces of the full (100-mm diameter) sapphire windows. Rayleigh signal levels have also increased because laser beam polarization is maintained after transmission through the fused silica, whereas previously, the polarization became elliptical and random after transmission through birefringent sapphire. Effectively, random polarization shifts reduce the efficiency of the Rayleigh scattering since the maximum scatter is obtained only with the laser beam polarized perpendicular to the camera collection direction. The net result is higher Rayleigh-scattering signal, and less background flare, when using the newer setup.

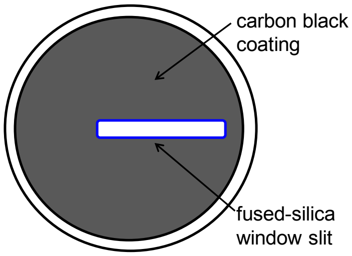

Figure B2: Metal port with fused-silica window insert (7×58 mm) for laser sheet transmission.

Another source of error that is evident in several regions of the image in Fig. B1 is Mie-scattering interference from the particles in the vaporized jet (not fuel droplets). Figure B1 is a relatively clean image, but other experimental conditions had more significant interference from particles. These particles could not be removed completely by repeated filtering and changing of the fuel. Images with many particles were not processed. For other images, particles were removed in post-processing using median filtering, or in more severe cases, by an inpainting routine [29]. These image processing routines are effective at removing outliers in data, which effectively forces the intensity distribution towards molecular scatterers, rather than bright, sparse particles. The effect of using the median filter to remove the particles was investigated in [23], where it was found that a bias error of approximately 1% may remain after filtering.

FUEL DECOMPOSITION EFFECTS

Fuel mixing experiments at high temperature and pressure may be subject to fuel decomposition, even if the ambient gases are inert. Fuel decomposition will affect Rayleigh scattering because as the fuel molecules break down, the Rayleigh cross-sections are not preserved. Once the Rayleigh cross-sections are unknown, it is not possible to relate the measured signal to the mixture fraction distribution. Similar problems may exist for LIF tracers, which further limits the quantification of mixing by LIF in addition to the issues of fluorescence calibration as a function of temperature and pressure introduced earlier. To illustrate the potential effects of fuel breakdown on the Rayleigh signal, we show the Rayleigh cross-section for several fuels and mixtures in Table B2.

Table B2. Rayleigh cross-sections for fuels, and stoichiometric mixtures (with air) of reactants and products.

Fuel	$\sigma_f \cdot 10^{-27}$ [cm^2]	$Z_{st} \cdot 10^{-2}$	$\sigma(Z_{st,R}) \cdot 10^{-27}$ [cm^2]	$\sigma(Z_{st,P}) \cdot 10^{-27}$ [cm^2]	@Z_{st}: $\frac{\sigma_R}{\sigma_P}$	@Z_{st}: $\frac{\sigma_R}{\sigma_{R,C3}}$
CH4	11.4	5.50	5.99	5.85	1.02	
C3H8	67.2	6.02	7.91	6.04	1.31	1.00
nC7	309.8	6.21	11.12	6.11	1.82	1.41
nC12	851.9	6.27	14.92	6.11	2.44	1.89
nC16	1508.0	6.29	18.19	6.10	2.98	2.30

The second column of Table B2 is the Rayleigh cross-section σ_f for selected fuels with carbon numbers ranging from 1 to 16, including those used in this study. The Rayleigh cross-section decreases significantly with decreasing carbon number. Similar results to that given in Table B2 are found in Ref. [22]. While the Rayleigh cross-section of a particular fuel may decrease if the fuel breaks down to a smaller carbon number, a more important question is how the Rayleigh cross-section of the mixture responds to such changes. For example, the Rayleigh cross-section of stoichiometric mixtures $\sigma(Z_{st,R})$ of pure fuel and air are given in column 4. Note that the change in $\sigma(Z_{st,R})$ is much less significant than that of σ_f, decreasing by only a factor of 3 (compared to 132 for σ_f) from C16 to C1. The reason for this difference is simple stoichiometry of mixtures. A small molecule like CH_4 has a stoichiometric number ratio $(N_a/N_f)_{st}$ of 20, while $(N_a/N_f)_{st}$ is 117 for $C_{16}H_{34}$. Therefore, $\sigma(Z_{st,R})$ is weighted more heavily by the Rayleigh cross-section of air mixed with the fuel. Nevertheless, Table 6 shows that the $\sigma(Z_{st,R})$ would decrease should the fuel molecule decompose, indicating that the Rayleigh signal still decreases.

A limit for fuel decomposition is that of complete combustion, or an equilibrium combustion product state. The Rayleigh cross-section for stoichiometric combustion product mixtures $\sigma(Z_{st,P})$, including major and minor species (e.g., CO_2, H_2O, CO) is shown in column 5. The column shows that $\sigma(Z_{st,P})$ essentially matches that of CH_4 as a reactant. In other words, complete combustion would have the same effect on the Rayleigh cross-section as fuel decomposition down to C1 species. Because of this, implementation of Rayleigh scattering for quantitative measurement in reacting environments is generally not feasible, except for light hydrocarbons like CH_4 [30]. For reacting environments, the Rayleigh signal decreases even further because gas density decreases with temperature rise. Therefore, a reduction in Rayleigh cross-section and gas density both tend to decrease Rayleigh signal. For non-reacting environments (*e.g.*, 0% O_2) the decrease in scattered signal intensity due to fuel decomposition would be less severe. Considering n-dodecane (nC12) as the fuel, Table B2 shows that the Rayleigh signal could decrease by approximately a factor of 2.4 if the fuel breaks down to

C1 species, or 1.9 if the fuel breaks down to C3 species. This exercise shows the limiting-case behavior if fuel decomposition does occur. For non-reacting mixtures, it would still be possible to perform qualitative visualization of mixing including jet spreading angle, but fully quantitative assessment would be suspect.

The discussion above highlights the need to assess whether or not fuel decomposition will occur, depending upon the ambient gas temperature and pressure of the operating condition. For this analysis, we use a simplified form of the two-stage Lagrangian (TSL) reacting-jet model [31], which is shown in Fig. B3. The TSL model incorporates detailed chemical kinetics while also simulating basic mixing processes important in turbulent gas-jet diffusion flames [31],or in this case, an evaporating spray. The TSL model typically incorporates two reactors, one representing the diffusion flame and the other representing an initially fuel-rich homogeneous reactor in the core of the jet. Mass from the surrounding ambient gas is transported into the reactors starting from the jet nozzle and moving downstream in a Lagrangian framework as shown in the schematic at the top. The model therefore captures basic features of how gas is entrained into jets, dependent upon the ambient and injector conditions. For example, temperature of the core increases with time as hot ambient gas is entrained into the jet, even when there is no heat release. The top of Fig. B3 shows this temperature increase for three different ambient temperatures, which also correspond to three different ambient densities (see caption). The limits for the time axis correspond to an approximate time required for the jet to penetrate completely across the 108-mm chamber.

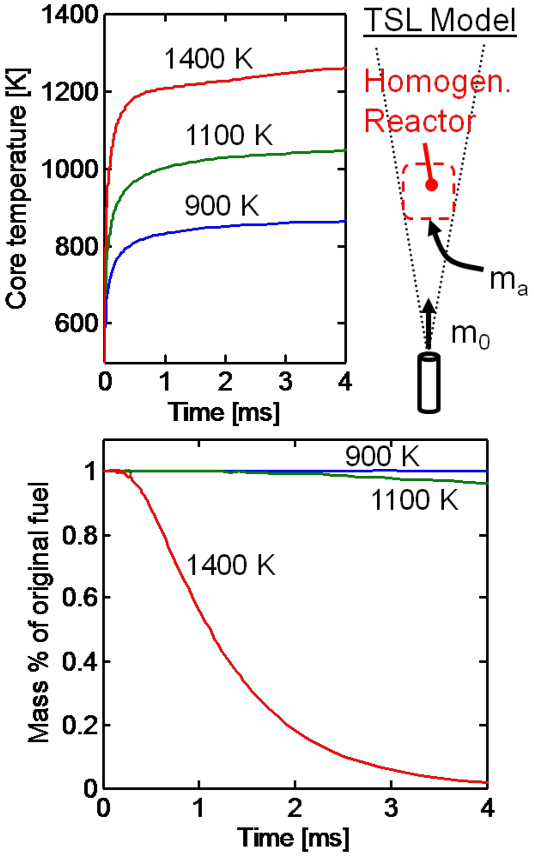

Figure B3: TSL reactor simulations of fuel-ambient mixing with detailed chemistry. Fuel is n-heptane, simulated for 150 MPa injection pressure. Ambient conditions, all with 0% O_2 (89.7% N_2, 6.5% CO_2, 3.8% H_2O): 1400 K, 7.6 kg/m^3, 3.1 MPa; 1100 K, 15.2 kg/m^3, 4.9 MPa; 900 K, 22.8 kg/m^3, 6.0 MPa.

The bottom of Fig. B3 shows the mass fraction of the original, parent fuel as the reactor moves downstream. In this case, we show a simulation using detailed n-heptane chemistry [31], but results do not change significantly for n-dodecane. The major conclusion is that minimal fuel decomposition is expected when the ambient temperature is less than 1100 K, but above this temperature, significant fuel decomposition is likely. Although fuel starts out at the nozzle quite cold, the entrained high-temperature gases raise the jet temperature. When the ambient temperature is 1100 K, mixture temperatures within the jet increase only slightly above 1000 K.

however, when the ambient temperature is 1400 K, mixture temperatures quickly exceed 1200 K and fuel breakdown occurs. Further analysis shows that the fuel breaks down into species that are high in carbon number and that may not reduce the Rayleigh cross-section as significantly as decomposition to C1 as discussed above (see Table B2). However, any fuel decomposition makes the mixing measurement by Rayleigh scattering suspect.

These detailed chemistry simulation results are in agreement with Rayleigh measurements performed in an evaporating n-decane spray in Ref. [22]. Ambient temperature was varied from 850 K to 1250 K, while holding ambient density constant at 9.6 kg/m^3. At 850 – 900 K, liquid droplets were still in the measurement domain. The Rayleigh signal was approximately constant at 1000 K to 1100 K, but it began to decrease at temperatures above 1200 K. This is supporting evidence that the TSL simulations provide a reasonable assessment as to whether fuel decomposition is an issue or not.